energies

MDPI

Article

A Common-Mode Voltage Suppression Strategy Based on Double Zero-Sequence Injection PWM for Two-Level Six-Phase VSIs

Li Zhao [1], Shoudao Huang [1,*], Yuan Gao [2] and Jian Zheng [3]

[1] College of Electrical and Information Engineering, Hunan University, Changsha 410082, China
[2] Department of Aerospace Engineering, Faculty of Engineering, University of Bristol, Queens Road, Bristol BS8 1QU, UK
[3] College of Electrical and Information Engineering, Hunan University of Technology, Zhuzhou 412007, China
* Correspondence: hsd1962@hnu.edu.cn; Tel.: +86-139-7511-3979

Abstract: A common-mode voltage (CMV) suppression strategy, namely double zero-sequence injection common-mode voltage (DZICMV), is proposed in this paper for an asymmetrical six-phase induction motor fed by two-level dual three-phase voltage source inverters (VSIs). In this strategy, the sinusoidal waveforms injected by double zero-sequence signals are employed as modulation signals, and two opposite triangular waveforms are used as carriers. The fundamental period is divided into 24 sectors. In each sector, the carrier used by the medium amplitude phase is distinct from the carriers used by the other two phases in each set of three-phase windings. Using this method, the zero vectors (000) and (111) in each set of three-phase windings can be eliminated, and the peak values of sub-CMV and total CMV can be reduced from $\pm U_{dc}/2$ to $\pm U_{dc}/6$. The experiment results show that the root mean square (RMS) value of common-mode leakage current in DZICMV can be reduced by 51.83% compared with the double zero-sequence injection PWM (DZIPWM) strategy. It is also found in the other four existing benchmark CMV suppression strategies that the peak values of sub-CMV therein are nearly all $\pm U_{dc}/2$, and only in the low linear modulation region could one of these strategies suppress sub-CMV peak values to $\pm U_{dc}/6$. However, the proposed DZICMV can suppress the sub-CMV peak values to $\pm U_{dc}/6$ in the whole linear modulation range. Moreover, the maximum linear modulation index of the DZICMV is 1.15, which is larger than that of the four benchmark strategies, whose maximum modulation index is 1.

Keywords: common-mode voltage (CMV); two-level six-phase VSIs; six-phase induction motors; total harmonic distortion (THD); common-mode leakage current

Citation: Zhao, L.; Huang, S.; Gao, Y.; Zheng, J. A Common-Mode Voltage Suppression Strategy Based on Double Zero-Sequence Injection PWM for Two-Level Six-Phase VSIs. *Energies* **2022**, *15*, 6242. https://doi.org/10.3390/en15176242

Academic Editor: Adolfo Dannier

Received: 12 July 2022
Accepted: 16 August 2022
Published: 26 August 2022

1. Introduction

Electric motor-driven systems (EMDSs) are widely used in industrial applications, such as liquid pumping, air conditioning, and heating [1]. Owing to transport electrification [2,3], EMDS is gaining more and more attention in the field of transport. The trend of electric vehicles (EVs) replacing fuel-powered vehicles is becoming irresistible. In 2015, the sales of passenger EVs were 450,000, while that of 2019 reached 2.1 million. The EV sales are expected to increase to 26 million by 2030 and possibly 54 million by 2040 [4]. The common-mode voltage (CMV) is unavoidable when the voltage source inverters (VSIs) are employed in EMDSs for EV or other applications [5]. The generated CMV leads to many problems, such as electromagnetic interference (EMI), deterioration of the motor winding insulation, shaft voltage, and bearing current [6,7]. With the introduction of wide-band gap (WBG) semiconductors, the switching frequencies of power devices will be higher, which leads to a worse situation [2]. In this context, how to suppress CMV has become one of the research hotspots.

In recent decades, various techniques for electric motors have been greatly developed, such as fuzzy control systems [8–10], motor optimization design [11,12], and modulation strategies [13]. In terms of mitigating the damages caused by CMV, there are hardware solutions and software solutions.

The hardware solutions mainly include redesigning the passive and active filters [14,15], modifying the topologies of the inverter [16,17], and installing a shaft grounding ring. In [14], a passive EMI filter is proposed to prevent high-frequency leakage current from flowing into the grounded heat sink and the grounded motor frame. An active EMI filter is proposed in [15], and it can be used for different applications regardless of its working voltage. Overall, inductors and capacitors are used in passive filters to suppress the high-frequency components, while active filters usually employ equipment to offset the common-mode current generated by CMV [18]. Bearing current can erode ball bearings and race walls, and thus, cause premature bearing failure [19]. To divert these currents before they damage the bearing, a motor shaft grounding ring is installed on the shaft between the motor and the gearbox [20]. The conductive microfibers of the ring are fixed up along its inner circumference, and thus, they can encircle the motor shaft. Since these microfibers provide a large contact surface, the shaft voltage can be released efficiently, and the bear current can be transferred well [19]. This solution is widely adopted by many companies, such as EVAG-Essener and HAVAG-Hallesche in Europe, and it is used in traction motors of some electric vehicles and light rail systems. For example, all-electric trams were installed with shaft grounding rings in 2007 to solve this bearing damage problem in Halle (Saale), Germany [20]. However, one of the main disadvantages of hardware solutions is that they increase the cost and complexity of the system.

As for the software solutions, lots of modulation strategies have been developed to suppress the CMV for different inverter topologies. The commonly used inverter topologies include three phases, five phases, and six phases. The following contents will briefly introduce the modulation strategies proposed by other scholars for these three topologies.

For three-phase VSIs, finite-control-set model predictive methods are studied in [21,22]. Although those methods can effectively suppress the CMV, they usually cause harmonic spread spectra of the output waveforms, which perplex the design of the output filter [23]. A carrier phase shifted method is proposed in [24], in which the three-phase carriers have a phase difference of one third carrier period to each other. However, it is only effective in the low modulation range. For SiC inverters used in electric vehicles, Ref. [25] showed that the high switching frequency of SiC inverters increases the high frequency of CMV noise, while having little effect on the magnitude of CMV. Since the More-Electric-Aircrafts (MEAs) have a high-reliability requirement of electric starter/generator (ESG) system, Ref. [26] proposed a modulation strategy based on the concept of a virtual-space vector. This strategy can mitigate the CMV and simultaneously balance the neutral-point voltage. Therefore, the reliability of the drive system is improved.

For five-phase VSIs, based on the space vector pulse width modulation (SVPWM) technique, six large voltage vectors are used in [27], and the peak value of CMV can be suppressed to $\pm 1/5\ U_{dc}$. Based on SVPWM and direct torque control (DTC), two methods, namely DTC1 and DTC2, are proposed by [28]. The CMV of DTC2 can be reduced by 80% in comparison with DTC1. Based on virtual voltage vectors (V^3s), two model predictive current control (MPCC) schemes are proposed in [29]. As the V^3s are composed of basic voltage vectors which generate small CMV, the CMV suppression can be realized. For the five-phase motor fed by a three-level neutral-point-clamped inverter, a successive cost function predictive torque control (SCF-PTC) method is proposed in [30], and a finite range of 31 voltage vectors is selected to eliminate the CMV. Reference [31] presents a method to eliminate the CMV for multilevel PWM inverters, but it is only suitable for an odd number of levels. Reference [32] proposes a method using three zero common-mode vectors to eliminate the CMV for multilevel inverters and this method is valid for both odd and even multilevel inverters. Ref. [33] proposed several different sigma-delta modulation strategies to obtain a constant CMV for a five-phase VSI. The vectors that generate a constant CMV with values of 0.1 V_{dc} or $-0.1\ V_{dc}$ are used by these strategies. Apart from the constant CMV level, they can also achieve a reduction in conducted EMI and a high-efficiency inverter operation. The drawback of these strategies is the maximum value of modulation index m is only 0.8, which is lower than the common SVPWM (m = 1.0515). Other six sigma-delta

modulation techniques are proposed for the five-phase VSI in [34]. These techniques can reduce the CMV peak-to-peak amplitude by 80%, and they can also decrease the number of CMV transitions, thus reducing the common-mode currents (CMCs). However, these techniques need to be implemented at high switching frequencies to obtain a low-voltage THD. In addition, Ref. [35] conducted a review of common multiphase motors topologies and their modulation techniques. This study shows that multiphase motors have the great potential to reduce CMV and multiphase systems are promising candidates to substitute conventional three-phase motor drives.

There are also some studies about the CMV suppression of two-level six-phase VSIs. A CMV suppression strategy named phase-shifted SPWM (PS-SPWM-1) was proposed by [36]. Six triangular carriers are used in this strategy, where the six carriers are shifted from each other by 1/6 carrier period T_c. Strategies PS-SPWM-2 and saw-tooth carrier-based sinusoidal PWM (SC-SPWM) are further proposed in [37]. In PS-SPWM-2, two opposite triangular waveforms are used as carriers. One triangular waveform is used as a carrier for one set of three-phase windings, and the other triangular waveform is used as the other set of three-phase windings. In the SC-SPWM, two saw-tooth waveforms are employed as carriers. Similar to PS-SPWM-2, one saw-tooth waveform is shared by one set of three-phase windings, and the other saw-tooth waveform is shared by the other set of windings. For the PS-SPWM-1 (in the high modulation region), PS-SPWM-2, and SC-SPWM, since the zero vectors (000) and (111) have existed in each set of three-phase windings, the sub-CMV peak values of these three strategies are not reduced, and remain at $\pm U_{dc}/2$. However, their total CMV peak values can be reduced because the six-phase switching states (000000) and (111111) are eliminated. For the zero CMV (ZCMV) method proposed by [38], the duty cycle of each phase is obtained by a sinusoidal modulation waveform, and an SVPWM method is used for the implementation of a digital signal processor (DSP). The turn-on/off moments of each leg in one set of three-phase windings are shifted and aligned to another leg in the other set of windings. Therefore, the peak value of total CMV can be suppressed to 0 in theory. However, the peak values of sub-CMV in ZCMV are still $\pm U_{dc}/2$, not suppressed. In addition, since the modulation signals of PS-SPWM-1, PS-SPWM-2, and SC-SPWM are six-phase sinusoidal waveforms, the maximum linear modulation index of these strategies is 1. For the ZCMV, the duty cycle of each phase is deduced by sinusoidal waveform, which determines the maximum linear modulation index, which is also 1. In contrast, by avoiding zero vectors (000) and (111) in each set of three-phase windings, the strategy proposed in this paper can suppress sub-CMV from $\pm U_{dc}/2$ to $\pm U_{dc}/6$ in the whole linear modulation range, which is smaller than that of the above four strategies. Furthermore, the maximum linear modulation index of the proposed strategy is 1.15, which is also better than the above strategies.

In this paper, a novel CMV suppression strategy, namely double zero-sequence injection common-mode voltage (DZICMV), is proposed for an asymmetrical six-phase induction motor fed by two-level dual three-phase voltage source inverters (VSIs). In this strategy, the carriers adopt two opposite triangular waveforms, and the modulation signals employ the sinusoidal waveforms injected by double zero-sequence signals. The fundamental period is divided into 24 sectors. In each sector, the carrier used by the medium amplitude phase is different from the carriers used by the other two phases in each set of three-phase windings. By this method, the zero vectors (000) and (111) in each set of three-phase windings are eliminated, and the peak values of sub-CMV and total CMV are, thus, reduced from $\pm U_{dc}/2$ to $\pm U_{dc}/6$. In the next section, the definitions of sub-CMV and total CMV are presented, and the possible values of sub-CMV and total CMV are deduced. In Section 3, the DZICMV is proposed. The rules of DZICMV are formulated in detail, and the validation of this strategy is given in the whole linear modulation range and the whole fundamental period. The simulation and experiment are carried out in Sections 4 and 5, respectively. In these two sections, waveforms such as CMV, common mode leakage current, and line voltage are shown. The main contributions of this work are summarized as follows:

(1) Compared with DZIPWM, the sub-CMV and total CMV peak values in the DZICMV are reduced by 66.67%, and the common-mode leakage current RMS value is reduced by 51.83% in the experiment. The torque and speed characteristics of these two strategies are close to each other.
(2) Compared with other modulation strategies, the proposed DZICMV also has an excellent CMV suppression effect. Specifically, the peak values of sub-CMV in PS-SPWM-1 (in high linear range), PS-SPWM-2, SC-SPWM, and ZCMV are $\pm U_{dc}/2$, while that in DZICMV are $\pm U_{dc}/6$, which is decreased by 66.67%.
(3) The maximum linear modulation index of DZICMV is 1.15, which is consistent with DZIPWM. It is larger than that of PS-SPWM-1, PS-SPWM-2, SC-SPWM, and ZCMV.
(4) In the high linear modulation region, the CMV suppression effect of DZICMV is much better than the PS-SPWM-1, although their line voltage THD values are close. Specifically, compared with PS-SPWM-1 in $0.76 < m < 1$, the peak values of sub-CMV in DZICMV can be reduced by 66.67%, and that of total-CMV can be reduced by 50%.
(5) Compared with the PS-SPWM-1, PS-SPWM-2, SC-SPWM, ZCMV, and DZIPWM in the whole linear modulation range, the sub-CMV RMS values in DZICMV are the lowest.
(6) Based on the same value of carrier frequency, the switching frequency of DZICMV is identical to that of PS-SPWM-1, PS-SPWM-2, SC-SPWM, and DZIPWM, but it is half of ZCMV. Therefore, the switching loss of DZICMV is less than that of ZCMV.
(7) By eliminating the zero vectors to suppress CMV in the proposed DZICMV, this general idea can be employed in other inverter topologies, e.g., the three-phase VSIs.

2. CMV Analysis for Six-Phase VSI

2.1. Basic Theory

The topology of an asymmetrical six-phase induction motor fed by two-level dual three-phase voltage source inverters (VSIs) is presented in Figure 1.

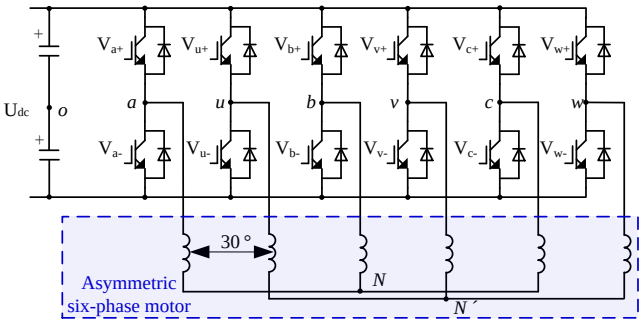

Figure 1. The topology of a six-phase motor fed by a VSI.

For two-level six-phase VSI, there are 64 space vectors in total. These vectors are defined by a decimal number that corresponds to a string of binary numbers, namely ($S_wS_vS_uS_cS_bS_a$). The S_j (j = a, b, . . . , w) denotes the switch state of up-branch in phase j, i.e., "$S_j = 0$" means OFF state and "$S_j = 1$" means ON state. According to the vector space decomposition (VSD) theory, the physical quantities, such as current, voltage, and flux, in the natural coordinate system are mapped onto three mutually perpendicular planes, namely d-q, x-y, and o_1-o_2. The d-q plane contains the fundamental component and the harmonic components with 12K ± 1 (K = 1, 2, 3, . . .) orders. Harmonic components with 6K ± 1 (K = 1, 3, 5, . . .) orders are mapped on the x-y plane. On the o_1-o_2 plane, the harmonic components with the order 6K ± 3 (K = 1, 3, 5, . . .) are mapped [39]. When the two neutral points are isolated from each other, all the vectors on the o_1-o_2 plane are at the origin [40]. On the d-q and x-y planes, there are 60 effective space vectors and four zero-vectors (namely 0, 7, 56, and 63), as shown in Figure 2.

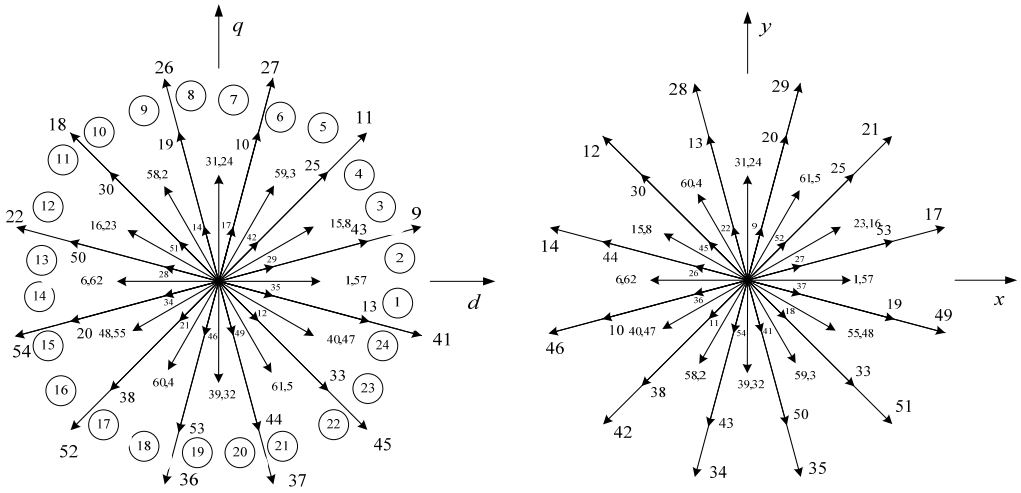

Figure 2. Space vectors in (**left**) *d*-*q* plane (**right**) *x*-*y* plane.

According to the power-constant transformation of VSD, the amplitudes of these vectors can be divided into four groups [41]: large vector V_L, medium-large vector V_{ML}, medium vector $V_{M,}$ and small vector V_S, as shown in Table 1. In addition, the definition of modulation index in this paper is the ratio of the fundamental amplitude of the phase voltage $|V_1|$ and half of the dc-link voltage U_{dc}.

Table 1. Amplitude of space vector for six-phase VSI.

Voltage Vector	Amplitude
V_L	1.113 U_{dc}
V_{ML}	0.816 U_{dc}
V_M	0.576 U_{dc}
V_S	0.297 U_{dc}

2.2. The Values of CMV

For the two-level six-phase VSI in which the two neutral points are isolated, the CMV can be classified as sub-CMV and total CMV. Similar to the three-phase VSI, the sub-CMV, namely V_{cm1} or V_{cm2} for each set of three-phase windings, is defined as the average value of the summed three-pole voltages [38], as shown in (1) and (2):

$$\begin{aligned} V_{cm1} &= \tfrac{1}{3}(V_{ao} + V_{bo} + V_{co}) \\ &= \tfrac{U_{dc}}{3}(S_a + S_b + S_c) - \tfrac{U_{dc}}{2} \end{aligned} \tag{1}$$

$$\begin{aligned} V_{cm2} &= \tfrac{1}{3}(V_{uo} + V_{vo} + V_{wo}) \\ &= \tfrac{U_{dc}}{3}(S_u + S_v + S_w) - \tfrac{U_{dc}}{2} \end{aligned} \tag{2}$$

where V_{ao}, V_{bo}, V_{co}, V_{uo}, V_{vo}, and V_{wo} are the pole voltages of six branches. As described above, S_j (j = a, b, . . . , w) denotes the switching state of the up-branch in phase j. Since the stray parameters of the motor are independent of how the winding ends are connected, the isolation or connection of the two neutral points does not affect the common-mode equivalent circuit model. Therefore, the total CMV V_{cm} can be defined as [38]:

$$\begin{aligned} V_{cm} &= \tfrac{1}{2}(V_{cm1} + V_{cm2}) \\ &= \tfrac{U_{dc}}{6}(S_a + S_b + S_c + S_u + S_v + S_w) - \tfrac{U_{dc}}{2} \end{aligned} \tag{3}$$

For the VSIs, "S_j = 0" and "S_j = 1" represent the OFF state and ON state, respectively. According to (1) and (2), all possible values of sub-CMV can be obtained, and are listed in

Table 2. As can be seen from (3), the total CMV is determined by the combination of two sub-CMVs. Therefore, the possible values of total CMV can be obtained, as shown in Table 3.

Table 2. CMV values generated by three-phase windings.

Switching State ($S_cS_bS_a$) **or** ($S_wS_vS_u$)	**Sub-CMV** (V_{cm1} **or** V_{cm2})
(000)	$-U_{dc}/2$
(111)	$U_{dc}/2$
(100) (010) (001)	$-U_{dc}/6$
(110) (101) (011)	$U_{dc}/6$

Table 3. The combinations of sub-CMV and total CMV for six-phase windings.

Group	**Sub-CMV** (V_{cm1},V_{cm2})	**Total CMV** (V_{cm})
1	($U_{dc}/2$, $U_{dc}/2$)	$U_{dc}/2$
2	($U_{dc}/2$, $-U_{dc}/2$) ($-U_{dc}/2$, $U_{dc}/2$)	0
3	($-U_{dc}/2$, $-U_{dc}/2$)	$-U_{dc}/2$
4	($U_{dc}/6$, $U_{dc}/6$)	$U_{dc}/6$
5	($U_{dc}/6$, $-U_{dc}/6$) ($-U_{dc}/6$, $U_{dc}/6$)	0
6	($-U_{dc}/6$, $-U_{dc}/6$)	$-U_{dc}/6$
7	($U_{dc}/2$, $U_{dc}/6$) ($U_{dc}/6$, $U_{dc}/2$)	$U_{dc}/3$
8	($-U_{dc}/2$, $U_{dc}/6$) ($U_{dc}/6$, $-U_{dc}/2$)	$-U_{dc}/6$
9	($U_{dc}/2$, $-U_{dc}/6$) ($-U_{dc}/6$, $U_{dc}/2$)	$U_{dc}/6$
10	($-U_{dc}/2$, $-U_{dc}/6$) ($-U_{dc}/6$, $-U_{dc}/2$)	$-U_{dc}/3$

3. The Proposed DZICMV Strategy

In the conventional double zero-sequence injection PWM (DZIPWM) strategy, the modulation signals are composed of sinusoidal waveforms injected by double zero-sequence signals, where the maximum linear modulation index can be increased to 1.15. The functions of sinusoidal waveforms and the double zero-sequence signals are expressed as (4) and (5), respectively. The harmonic components in the double zero-sequence signals are in the order 6K $\pm$ 3 (K = 1, 3, 5, ...) and are mapped on the o_1-o_2 plane. The modulation signal functions of DZIPWM are given as (6), and they are used to compare with a triangular carrier to generate the PWM waveforms. These characteristics are utilized as a theoretical basis of the proposed DZICMV strategy.

$$\begin{cases} u'_a = U_{om} \cdot \cos(\omega t) \\ u'_b = U_{om} \cdot \cos(\omega t - \frac{2}{3}\pi) \\ u'_c = U_{om} \cdot \cos(\omega t + \frac{2}{3}\pi) \\ u'_u = U_{om} \cdot \cos(\omega t - \frac{1}{6}\pi) \\ u'_v = U_{om} \cdot \cos(\omega t - \frac{5}{6}\pi) \\ u'_w = U_{om} \cdot \cos(\omega t + \frac{1}{2}\pi) \end{cases} \tag{4}$$

$$\begin{cases} u_{no1} = -\frac{1}{2}\left(\max\left(u'_a, u'_b, u'_c\right) + \min\left(u'_a, u'_b, u'_c\right)\right) \\ u_{no2} = -\frac{1}{2}\left(\max(u'_u, u'_v, u'_w) + \min(u'_u, u'_v, u'_w)\right) \end{cases} \tag{5}$$

$$\begin{cases} u_{j1} = u'_{j1} + u_{no1} \quad (j1 = a, b, c) \\ u_{j2} = u'_{j2} + u_{no2} \quad (j2 = u, v, w) \end{cases} \tag{6}$$

where U_{om} and ω are the amplitude and angular frequency, respectively, u_{no1} and u_{no2} are the zero-sequence signals, and u_{j1} and u_{j2} are the modulation signals of two sets of three-phase windings for the DZIPWM.

3.1. The Proposed DZICMV

In the DZIPWM, due to the existing zero vectors for six-phase windings, namely (000000) and (111111), the peak values of both sub-CMV and total CMV are $\pm U_{dc}/2$. As can be seen from Tables 2 and 3, the possible values of sub-CMV are $\pm U_{dc}/2$ and $\pm U_{dc}/6$, while the possible values of total CMV are $\pm U_{dc}/2$, $\pm U_{dc}/3$, $\pm U_{dc}/6$, and 0. Therefore, compared with DZIPWM, the sub-CMV of any newly proposed strategy can be reduced by 66.67% at most, while the total CMV can be reduced by 33.33, 66.67 and 100%, respectively.

If the two sub-CMVs are not equal to $\pm U_{dc}/2$, the possible combinations of sub-CMV and total CMV are the Groups 4, 5, and 6 of Table 3, in which the values of total CMV are 0 and $\pm U_{dc}/6$. In this case, the peak values of both sub-CMV and total CMV are $\pm U_{dc}/6$. To ensure the sub-CMV values are not equal to $\pm U_{dc}/2$, according to Table 2, the zero vectors in each set of three-phase windings ((000) and (111)) should be eliminated. For that purpose, the rules of the proposed DZICMV are designed as follows.

The modulation signals also employ the sinusoidal waveforms injected by double zero-sequence signals, as given in (6), but the fundamental period is divided into 24 sectors. The sector number is identified by Arabic letters, as illustrated in Figure 3, and the number of sectors corresponding to the *d*-*q* plane is shown in Figure 2. In each sector, according to the instantaneous values of the modulation signals, u_a, u_b, and u_c are sorted from high to low as $u_{1\max}$, $u_{1\mathrm{mid}}$, and $u_{1\min}$, respectively. Similarly, u_u, u_v, and u_w are sorted from high to low as $u_{2\max}$, $u_{2\mathrm{mid}}$, and $u_{2\min}$, respectively. Two opposite triangular carriers are used in DZICMV, namely Carrier-1 and Carrier-2, whose phases are shifted from each other by a half of the carrier period T_c, as shown in Figure 4. Then, $u_{1\max}$, $u_{1\min}$, and $u_{2\mathrm{mid}}$ share the Carrier-1, and $u_{2\max}$, $u_{2\min}$, and $u_{1\mathrm{mid}}$ share the Carrier-2. As a result, a total of 24 sectors produce four types of schemes: (1) when the reference space vector V_{ref} is located in the 1st, 2nd, 9th, 10th, 17th, and 18th sectors, the switching state meets the Type I of scheme shown in Figure 4a; (2) when V_{ref} is located in the 3rd, 4th, 11th, 12th, 19th, and 20th sectors, the switching state meets the Type II shown in Figure 4b; (3) when V_{ref} is located in the 5th, 6th, 13th,14th, 21st, and 22nd sectors, the switching state meets the Type III shown in Figure 4c; (4) when V_{ref} is located in the 7th, 8th, 15th, 16th, 23rd, and 24th sectors, the switching state meets the Type IV shown in Figure 4d. These four types are summarized in Table 4.

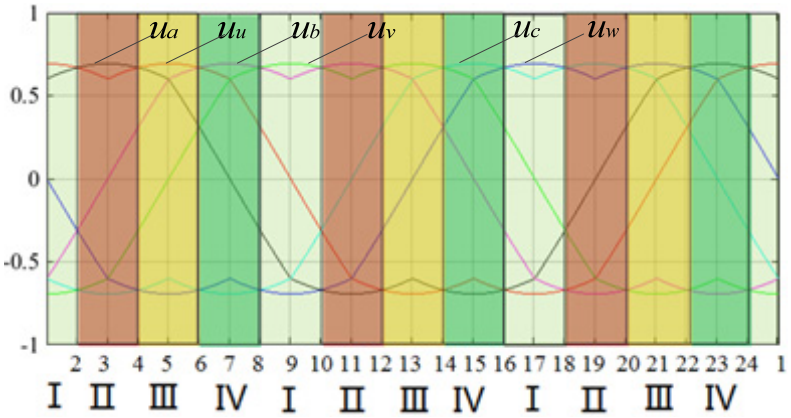

Figure 3. Region division in a fundamental period for the DZICMV.

Table 4. Relationship between sectors and the four types of schemes in the DZICMV.

Type	Sector	Type	Sector
I	1,2,9,10,17,18	III	5,6,13,14,21,22
II	3,4,11,12,19,20	IV	7,8,15,16,23,24

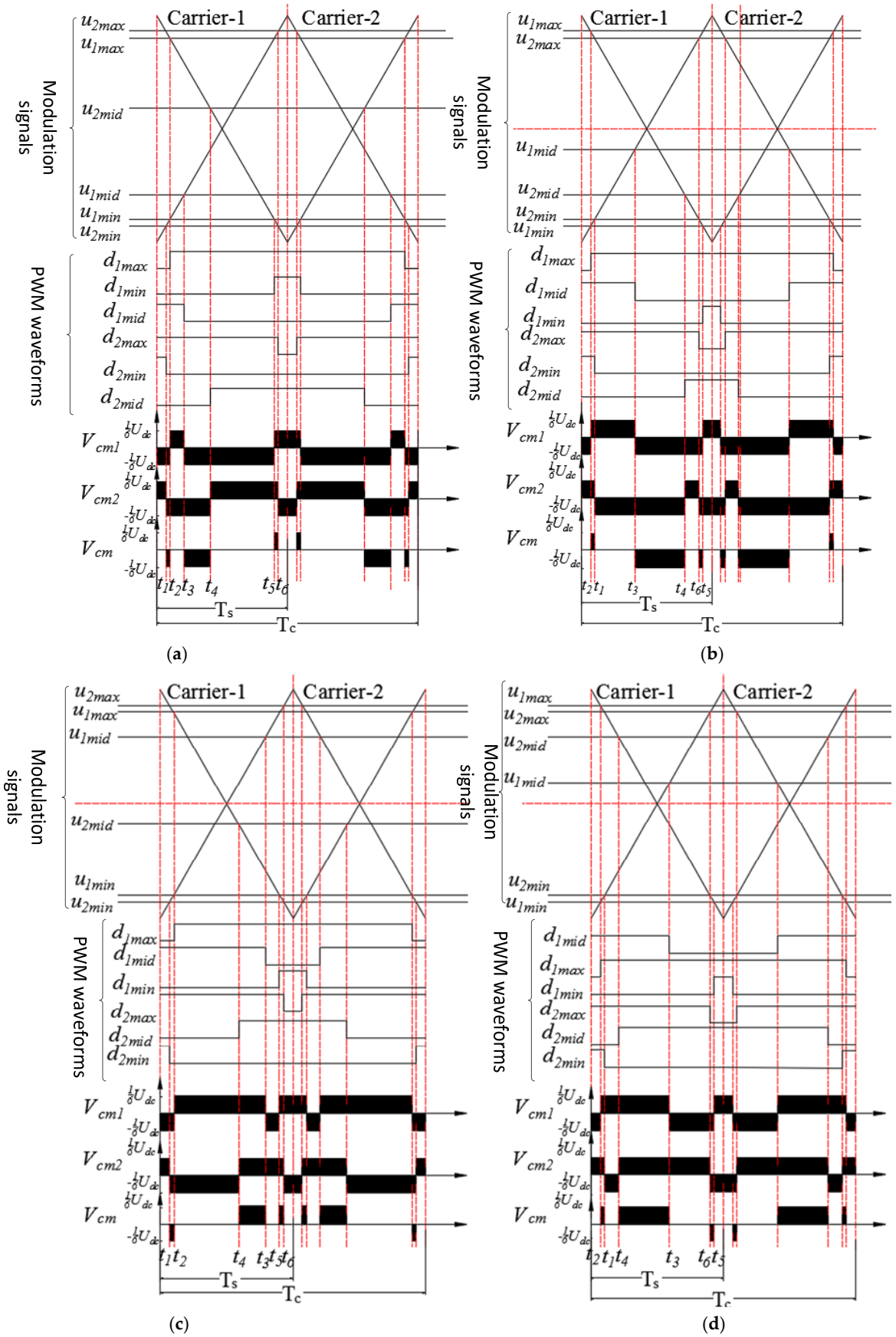

Figure 4. Four types of schemes in the DZICMV: (**top**) modulation signals and carriers, (**middle**) PWM waveforms, (**bottom**) two sub-CMVs and total CMV for (**a**) Type I; (**b**) Type II; (**c**) Type III; (**d**) Type IV.

According to (1)–(3), the values of sub-CMV and total CMV for every interval of a carrier period T_c can be obtained, as shown at the bottom of Figure 4. The peak values of both sub-CMV and total CMV in DZICMV are $\pm U_{dc}/6$.

3.2. Validation of DZICMV

The following contents are to verify that the schemes shown in Figure 4 can pass through the whole fundamental period and whole linear modulation range. For a triangular carrier, the duty cycle d_j of phase j can be expressed as [42]:

$$d_j = \frac{1}{2} + \frac{u_j}{U_{dc}} (j = a, b, c, u, v, w) \tag{7}$$

Substituting (6) into (7), the duty cycle of each phase can be obtained. According to Figure 4, the transition moments of six legs can be expressed as:

$$\begin{array}{l} t_1 = d_{2\min} \cdot T_s \\ t_2 = (1 - d_{1\max}) \cdot T_s \\ t_3 = d_{1\mathrm{mid}} \cdot T_s \\ t_4 = (1 - d_{2\mathrm{mid}}) \cdot T_s \\ t_5 = (1 - d_{1\min}) \cdot T_s \\ t_6 = d_{2\max} \cdot T_s \end{array} \tag{8}$$

where T_s is a sampling period.

To eliminate zero vector (000) and (111) in each set of three-phase windings, as shown in Figure 4, the phases a, b, and c should satisfy (9) for these four types of schemes:

$$t_2 < t_3 < t_5 \tag{9}$$

Similarly, the phases u, v, and w should satisfy (10) for these four types of schemes:

$$t_1 < t_4 < t_6 \tag{10}$$

Furthermore, if (11)–(14) are satisfied in the whole fundamental period and whole linear modulation range, it means the space vectors generated by PWM waveforms are constant, and they are not varied against the change of modulation index in each sector.

For the Type I:

$$0 < t_1 < t_2 < t_3 < t_4 < t_5 < t_6 < T_s \tag{11}$$

For the Type II:

$$0 < t_2 < t_1 < t_3 < t_4 < t_6 < t_5 < T_s \tag{12}$$

For the Type III:

$$0 < t_1 < t_2 < t_4 < t_3 < t_5 < t_6 < T_s \tag{13}$$

For the Type IV:

$$0 < t_2 < t_1 < t_4 < t_3 < t_6 < t_5 < T_s \tag{14}$$

Substituting (8) into (11), one can obtain:

$$\begin{cases} L_1 = -u_{1\max} - u_{2\min} > 0 \\ L_2 = u_{1\max} + u_{1\mathrm{mid}} > 0 \\ L_3 = -u_{1\mathrm{mid}} - u_{2\mathrm{mid}} > 0 \\ L_4 = u_{2\mathrm{mid}} - u_{1\min} > 0 \\ L_5 = u_{1\min} + u_{2\max} > 0 \end{cases} \tag{15}$$

Substituting (8) into (12), one can obtain:

$$\begin{cases} L_1 = u_{1\max} + u_{2\min} > 0 \\ L_2 = -u_{2\min} + u_{1\mathrm{mid}} > 0 \\ L_3 = -u_{1\mathrm{mid}} - u_{2\mathrm{mid}} > 0 \\ L_4 = u_{2\mathrm{mid}} + u_{2\max} > 0 \\ L_5 = -u_{1\min} - u_{2\max} > 0 \end{cases} \tag{16}$$

Substituting (8) into (13), one can obtain:

$$\begin{cases} L_1 = -u_{1\max} - u_{2\min} > 0 \\ L_2 = u_{1\max} - u_{2\mathrm{mid}} > 0 \\ L_3 = u_{1\mathrm{mid}} + u_{2\mathrm{mid}} > 0 \\ L_4 = -u_{1\mathrm{mid}} - u_{1\min} > 0 \\ L_5 = u_{1\min} + u_{2\max} > 0 \end{cases} \tag{17}$$

Substituting (8) into (14), one can obtain:

$$\begin{cases} L_1 = u_{1\max} + u_{2\min} > 0 \\ L_2 = -u_{2\min} - u_{2\mathrm{mid}} > 0 \\ L_3 = u_{1\mathrm{mid}} + u_{2\mathrm{mid}} > 0 \\ L_4 = -u_{1\mathrm{mid}} + u_{2\max} > 0 \\ L_5 = -u_{1\min} - u_{2\max} > 0 \end{cases} \tag{18}$$

Although the definitions of L_x (x = 1, 2, 3, 4, and 5) for these four types of schemes are different, the proposed strategy can meet the limits of (11)–(14) when all the L_x are larger than 0. Based on that, the different L_x are drawn in the whole linear modulation range and a whole fundamental period, as shown in Figure 5.

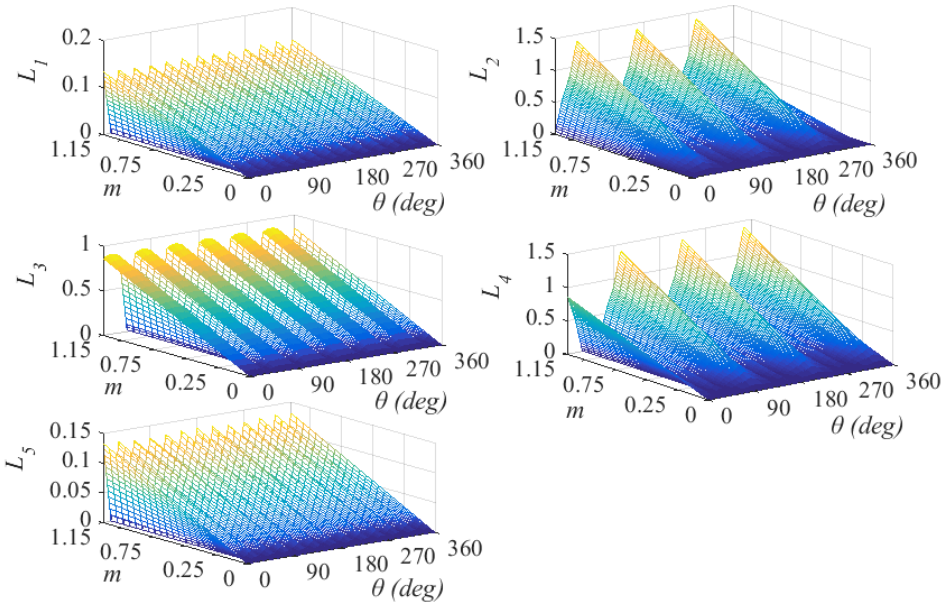

Figure 5. The values of L_x (x = 1, 2, 3, 4 and 5) in a whole fundamental period and whole linear modulation range.

All values of L_x are larger than 0. On the other hand, the DZICMV also satisfies (9) and (10). Specifically, the zero vectors, namely (000) and (111), are eliminated in each three-phase windings, and the vectors generated in each sector will not change along with modulation index changes. For example, in the 1st sector, the switching sequence is 28-12-13-9-41-43-35 for a sampling period T_s, and these vectors (including the sequence)

will be the same when m changes. This characteristic of constant vectors provides convenience and the possibility of studying other characteristics, such as harmonic flux trajectories, harmonic distortion factor (HDF), and current ripple, while they are beyond the scope of this paper.

3.3. Comparison of the CMV Suppression Effect

Apart from the conventional DZIPWM, other four modulation strategies, namely PS-PWM-1, PS-PWM-2, SC-SPWM, and ZCMV, are also considered as the benchmarks of the proposed DZICMV. CMV peak values and the reduced percentage ratio of these strategies (compared with DZIPWM) are listed in Table 5.

Table 5. The CMV peak values and the percentage of decrease.

Strategy	Sub-CMV	Total CMV
PS-SPWM-1 ($0.76 < m < 1$)	$\pm U_{dc}/2$ ($\downarrow 0$)	$\pm U_{dc}/3$ ($\downarrow 33.33\%$)
PS-SPWM-1 ($0.67 < m < 0.76$)	$\pm U_{dc}/2$ ($\downarrow 0$)	$\pm U_{dc}/6$ ($\downarrow 66.67\%$)
PS-SPWM-1 ($0 < m < 0.67$)	$\pm U_{dc}/6$ ($\downarrow 66.67\%$)	$\pm U_{dc}/6$ ($\downarrow 66.67\%$)
PS-SPWM-2 ($0 < m < 1$)	$\pm U_{dc}/2$ ($\downarrow 0$)	$\pm U_{dc}/6$ ($\downarrow 66.67\%$)
SC-SPWM ($0 < m < 1$)	$\pm U_{dc}/2$ ($\downarrow 0$)	$\pm U_{dc}/6$ ($\downarrow 66.67\%$)
ZCMV ($0 < m < 1$)	$\pm U_{dc}/2$ ($\downarrow 0$)	0 ($\downarrow 100\%$)
DZIPWM ($0 < m < 1.15$)	$\pm U_{dc}/2$	$\pm U_{dc}/2$
DZICMV ($0 < m < 1.15$)	$\pm U_{dc}/6$ ($\downarrow 66.67\%$)	$\pm U_{dc}/6$ ($\downarrow 66.67\%$)

Among these strategies, almost all of their sub-CMV peak values are $\pm U_{dc}/2$, and only PS-SPWM-1can suppress them to $\pm U_{dc}/6$ in the low modulation range ($0 < m < 0.67$). In contrast, the proposed DZICMV can suppress peak values of sub-CMV to $\pm U_{dc}/6$ in the whole linear modulation range. The peak values of total CMV in DZICMV are also $\pm U_{dc}/6$, which is consistent with PS-SPWM-2 and SC-SPWM. Compared with DZIPWM, they are also decreased by 66.67%. In addition, the maximum linear modulation index of the DZICMV is 1.15, which is larger than that of PS-PWM-1, PS-PWM-2, SC-SPWM, and ZCMV.

3.4. Comparison of Switching Frequency

As can be seen from Figure 4, for the proposed DZICMV, the turn-on/off times for six-phase legs of VSI in each carrier period T_c is 12. It is consistent with that of PS-SPWM-1, PS-SPWM-2, SC-SPWM, and DZIPWM, but it is half of the ZCMV's turn-on/off times. Therefore, the switching loss of DZICMV should be less than that of ZCMV. Furthermore, in the ZCMV, since there are more than twice turn-on/off in each leg during every carrier period T_c, it is difficult to implement DSP.

4. Simulation

To verify the CMV suppression effect of the proposed DZICMV and other strategies, the model of a six-phase induction motor fed by a two-level six-phase VSI was built using the MATLAB/Simulink platform. In the simulation, the motor control method was the rotor field-oriented control (FOC), and the control block diagram is shown in Figure 6. The motor parameters are shown in Table 6. The motor started with no-load, and the command speed n^* was 2400 r/min. A load torque T_L = 15 N·m was applied at 0.45 s, and the n^* then changed to 2280 r/min at 0.65 s. These three working conditions of the motor are shown in Table 7. The carrier frequency f_c was set to 5 kHz, and dc-link voltage U_{dc} was 360 V.

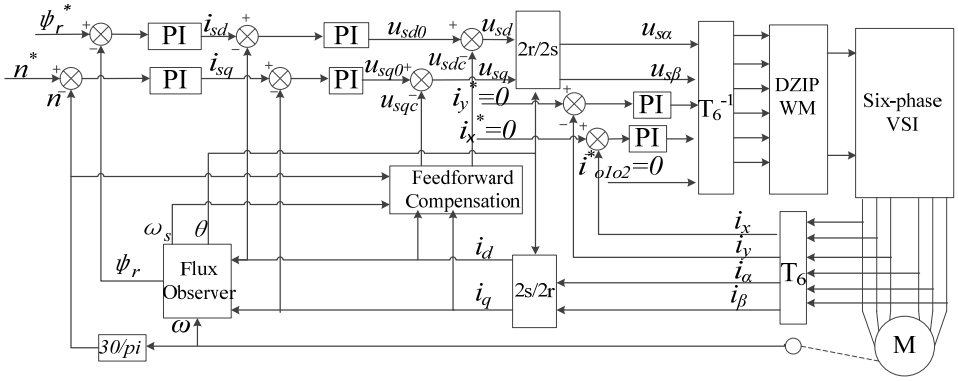

Figure 6. The control block diagram of FOC.

Table 6. Parameters of the induction motor.

Symbol	Parameter	Value
R_s	Stator resistance	1.5 Ω
L_{lr}'	Rotor leakage inductance	0.014 H
R_r	Rotor resistance	1.12 Ω
L_m	Mutual inductance	0.262 H
L_{lsdq}	Stator leakage inductance in *d-q* plane	0.0124 H
L_{lsxy}	Stator leakage inductance in *x-y* plane	0.0062 H
P	Number of pole pairs	1

Table 7. The motor working conditions.

Working Conditions	Time *t*(s)	T_L (N·m)	n^* (r/min)
Condition 1	0.4~0.45	0	2400
Condition 2	0.45~0.65	15	2400
Condition 3	0.65~0.8	15	2280

The second working condition, namely Condition 2, is taken as an example to compare the CMV suppression effect of the DZIPWM and DZICMV, as shown in Figures 7–10.

Figures 7 and 8 show the CMV waveforms of the DZIPWM and DZICMV, respectively. The number of sub-CMV levels is 4 for DZIPWM, while it is 2 for DZICMV. The level number of total CMV is 7 for DZIPWM, while it is 3 for DZICMV. There are five carrier periods shown in the enlarged view of Figures 7 and 8. During this time, both V_{cm1} and V_{cm2} of DZIPWM change 31 times, which is consistent with that of DZICMV. However, at around 0.619 s in Figure 7, the V_{cm} changing value of DZIPWM is $U_{dc}/3$, which is larger than that of $U_{dc}/6$ in DZICMV. A high changing value will cause high dv/dt, thereby producing a high transient common-mode leakage current. The peak values of sub-CMV and total CMV in the DZIPWM are ±180 V, which are $\pm U_{dc}/2$, while they are ±60 V ($\pm U_{dc}/6$) in the DZICMV. Therefore, the peak values of both the sub-CMV and total CMV in the DZICMV are reduced by 66.67%. As discussed, the main reason is that the zero vectors (000) and (111) in each set of three-phase windings are eliminated in DZICMV. The simulation results of DZICMV are identical to the analysis results in Figure 4.

Fast Fourier Transform (FFT) analysis was performed on the sub-CMV and total CMV for both strategies, as shown in Figures 9 and 10.

The maximum harmonic amplitudes at integer multiples of the carrier frequency sidebands are listed in Table 8.

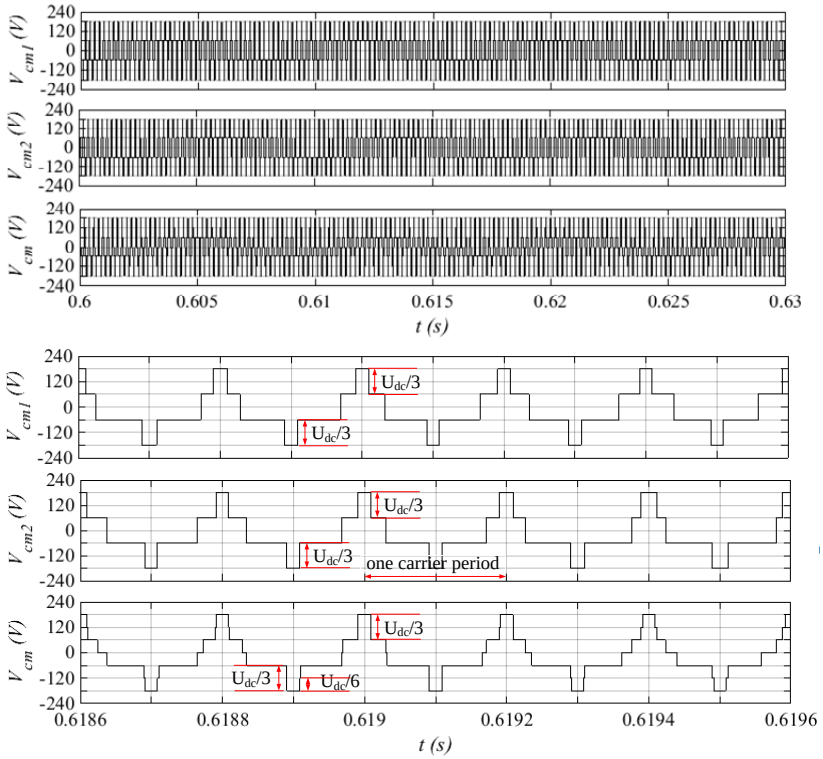

Figure 7. Simulation results of CMV for the DZIPWM strategy: two sub-CMVs V_{cm1} and V_{cm2}, total CMV V_{cm}.

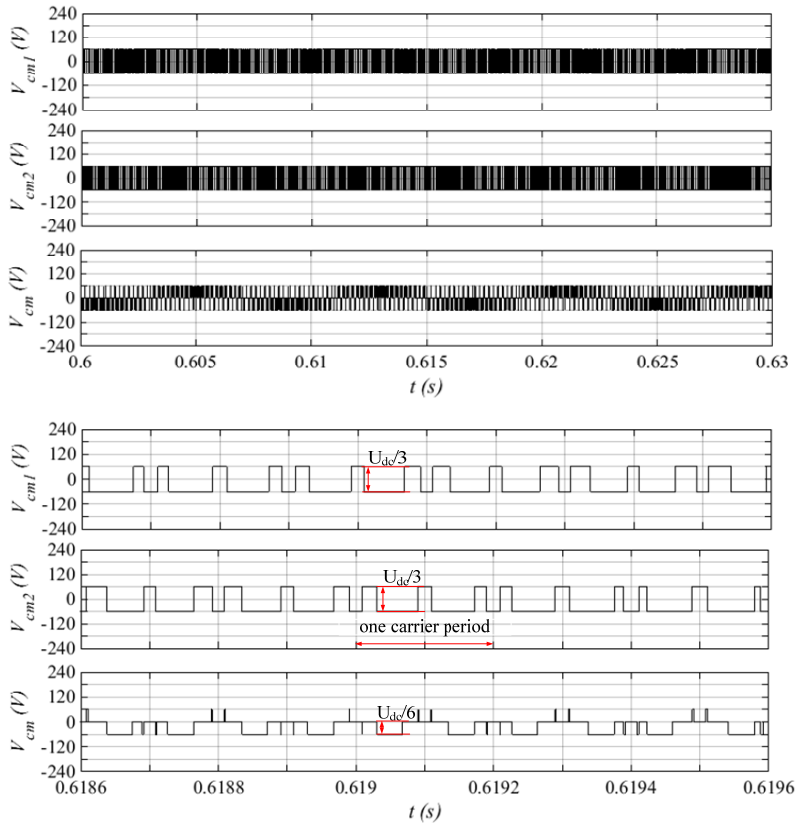

Figure 8. Simulation results of CMV for the proposed DZICMV strategy: two sub-CMVs V_{cm1} and V_{cm2}, total CMV V_{cm}.

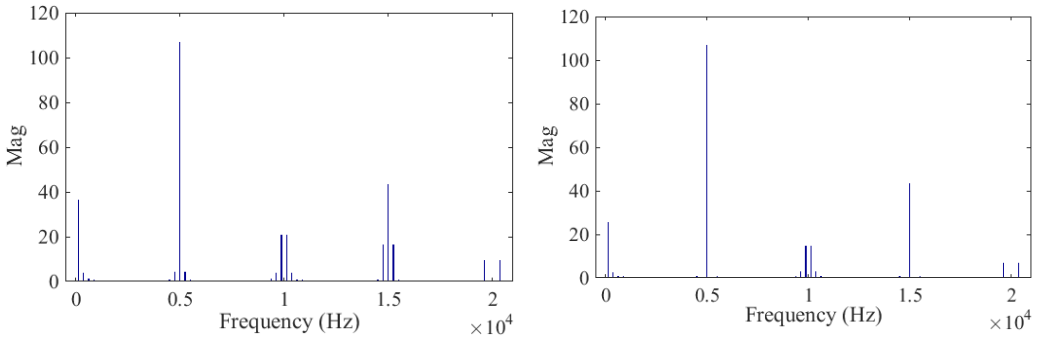

Figure 9. FFT analysis of CMV for DZIPWM: (**left**) the sub-CMV V_{cm1}; (**right**) total CMV V_{cm}.

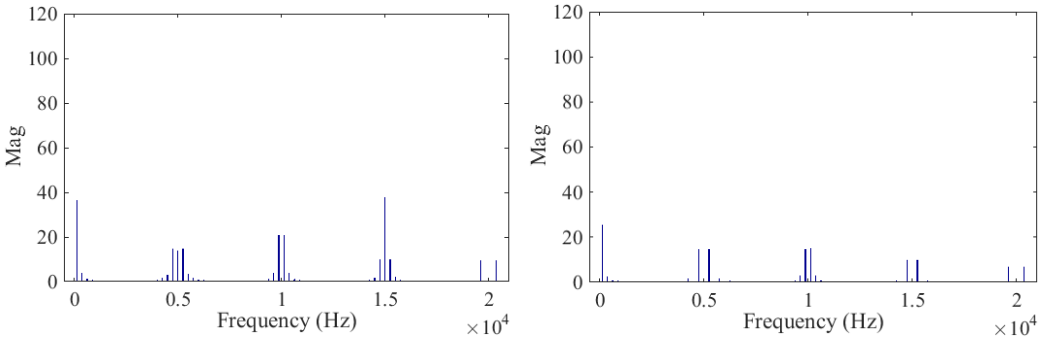

Figure 10. FFT analysis of CMV for DZICMV: (**left**) the sub-CMV V_{cm1}; (**right**) total CMV V_{cm}.

Table 8. The CMV maximum harmonic amplitudes for DZIPWM and DZICMV.

	Sub-CMV V_{cm1} (V)		**Total CMV V_{cm} (V)**	
	DZIPWM	**DZICMV**	**DZIPWM**	**DZICMV**
The third harmonic	36.11	36.10	25.54	25.51
5 kHz (sideband)	106.83	14.70	106.83	14.67
10 kHz (sideband)	20.86	20.83	14.75	14.72
15 kHz (sideband)	43.15	37.48	43.16	9.96
20 kHz (sideband)	9.42	9.40	6.65	6.63

Due to the existence of slip in the asynchronous motor, the corresponding fundamental frequency at n^* = 2400 r/min is 41.6667 Hz instead of 40 Hz. Therefore, the frequency value of the third harmonic can be obtained. As can be seen from Figures 9 and 10, the harmonic components of the CMV mainly focus on the three times the fundamental frequency and integer multiples of the carrier frequency. The content of the third harmonic is significant, which is caused by the injected double zero-sequence signal, as shown in (6). The maximum harmonic amplitude of DZICMV at each integer multiple carrier frequency sideband is lower than that of DZIPWM, especially at the first carrier frequency sideband (5 kHz). Therefore, the CMV harmonic amplitude can be effectively reduced by the DZICMV.

The simulation results about motor characteristics are shown in Figures 11–16.

Figures 11 and 12 show the waveforms of electromagnetic torque T_e and rotor speed n for these two strategies, respectively. In general, these two strategies have good dynamic following characteristics of the torque and speed when the working conditions change. As can be seen from the enlarged view of the torque, the torque ripple of DZICMV is slightly larger than that of DZIPWM.

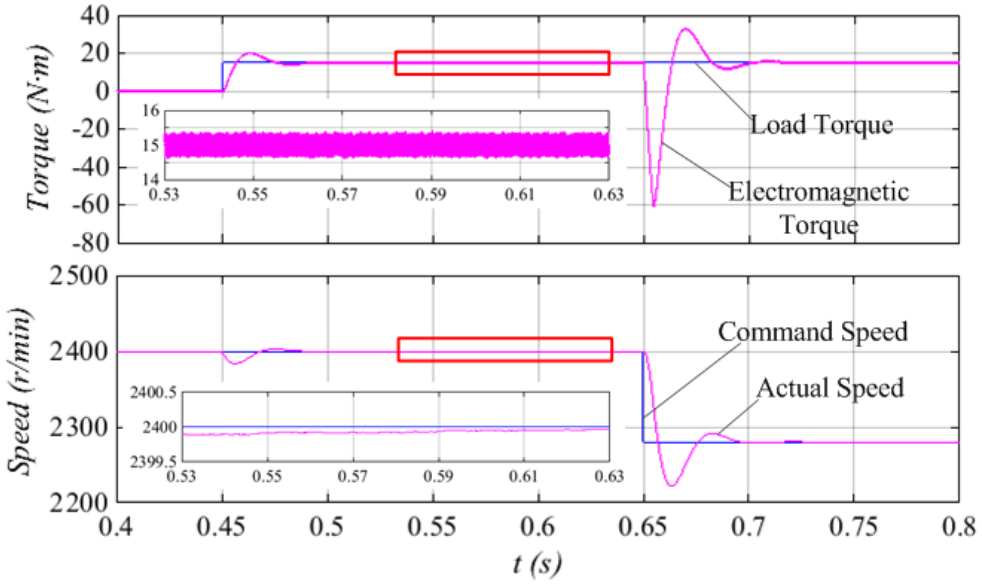

Figure 11. Simulation results of electromagnetic torque T_e and rotor speed n for the DZIPWM.

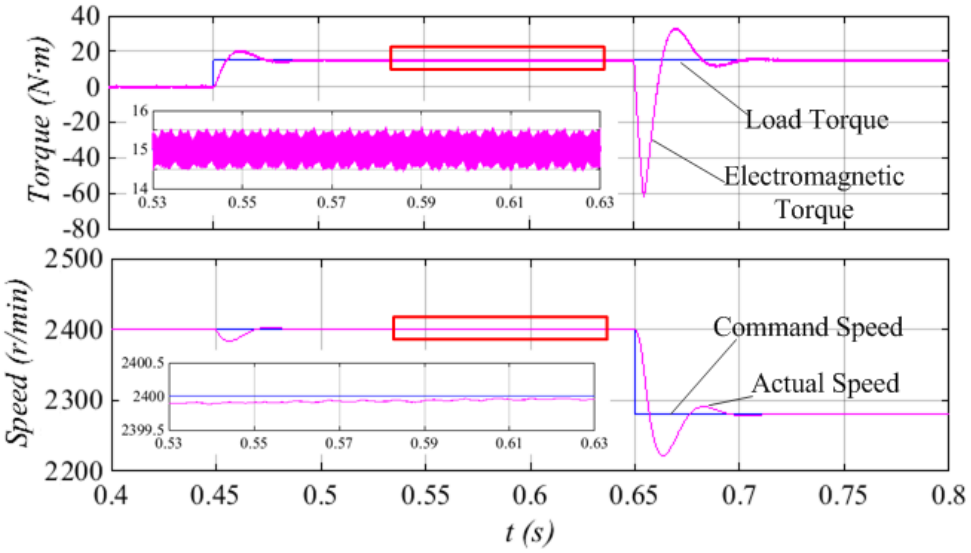

Figure 12. Simulation results of electromagnetic torque T_e and rotor speed n for the DZICMV.

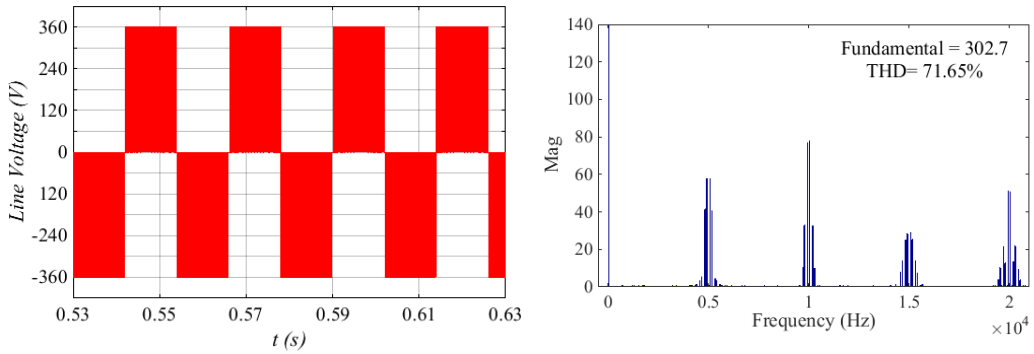

Figure 13. Simulation waveforms of line voltage u_{ab} for DZIPWM at m = 0.9703: (**left**) line voltage u_{ab} (**right**) the FFT analysis of u_{ab}.

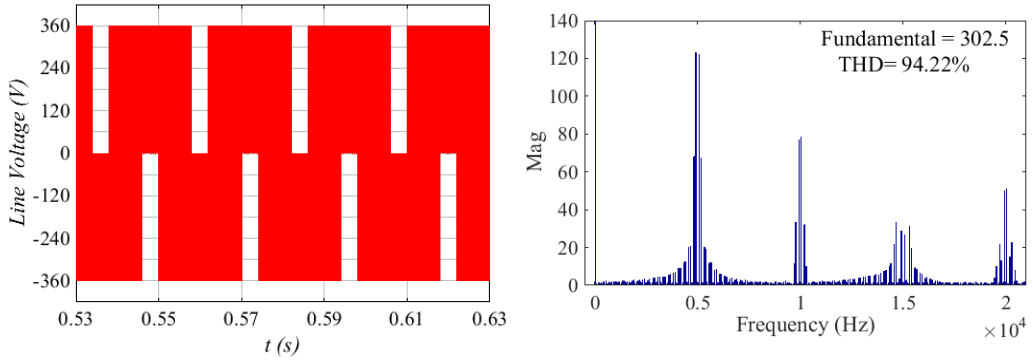

Figure 14. Simulation waveforms of line voltage u_{ab} for DZICMV at m = 0.9703: (**left**) line voltage u_{ab} (**right**) the FFT analysis of u_{ab}.

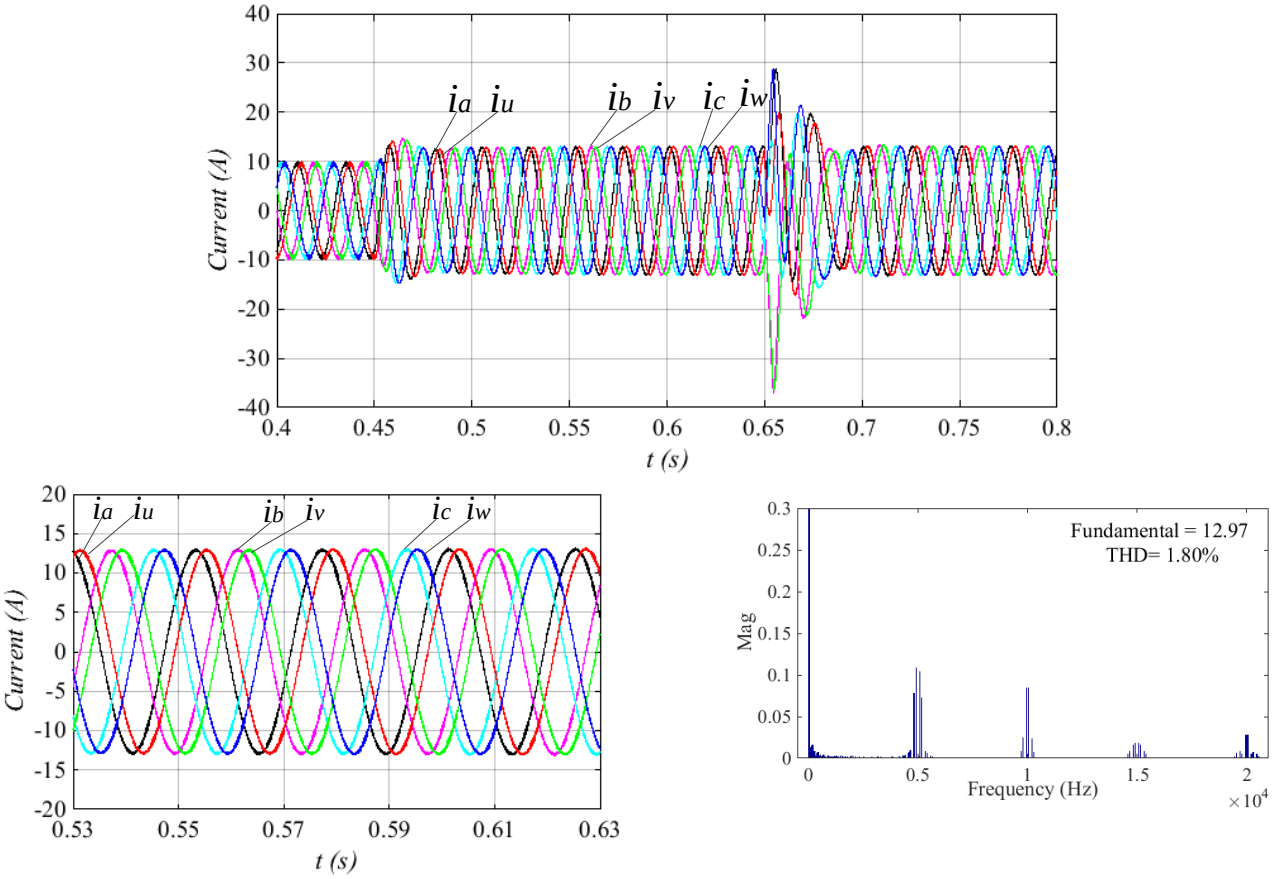

Figure 15. Simulation results of the six-phase current and the FFT analysis of the steady state current i_a for DZIPWM.

Corresponding to Condition 2, Figures 13 and 14 show the line voltage waveforms and FFT analysis of both strategies. The fundamental line voltage values of these two strategies are 302.7 and 302.5 V, respectively, and thus, the modulation index m is about 0.9703. The spectrums of FFT analysis mainly include the first four carrier frequency sidebands, and the THD value of DZICMV is higher than that of DZIPWM. The DZICMV is characterized by a much richer spectrum of line voltage u_{ab}, especially at the sideband of the first carrier frequency (5 kHz). Two opposite carriers are used in each set of three-phase windings of DZICMV, which results in different voltage harmonics from DZIPWM.

Compared with DZIPWM (Figure 15), the currents of DZICMV (Figure 16) perform a slight harmonic distortion, and the current THD value is also larger than that of DZIPWM. This is caused by the line voltage distortion in DZICMV, as shown in Figure 14. However,

as stated in [36], there is a tradeoff between the decrease of CMV and the harmonic increase of the output voltage and current.

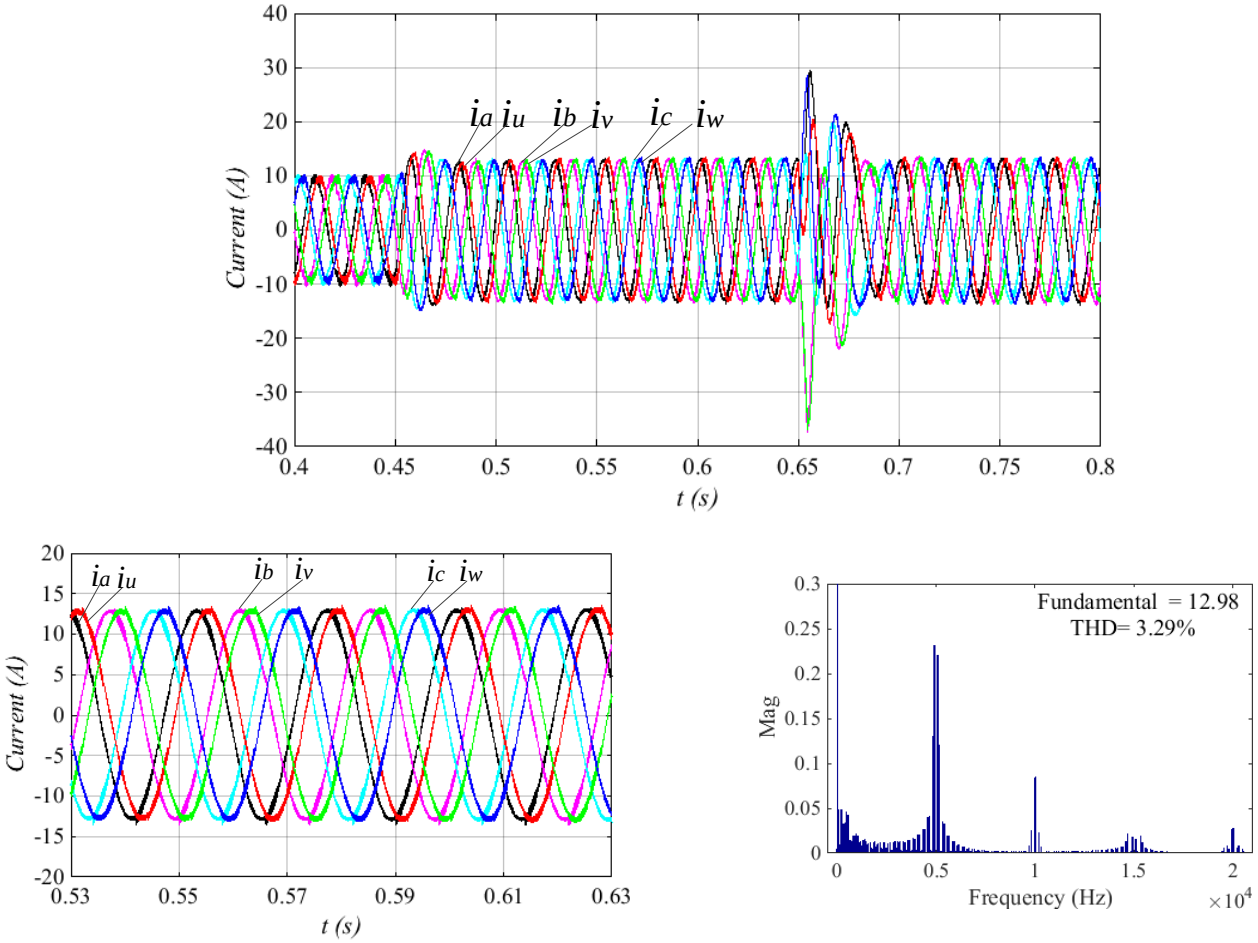

Figure 16. Simulation results of the six-phase current and the FFT analysis of the steady state current i_a for DZICMV.

In the closed-loop control, the modulation index is jointly determined by the load torque and the command speed. To obtain the RMS of CMV and the THD of line voltage at different accurate modulation indexes, the following two simulations were performed under the open-loop control, as shown in Figures 17 and 18. The carrier frequency was set to 5 kHz, and the fundamental frequency was 40 Hz.

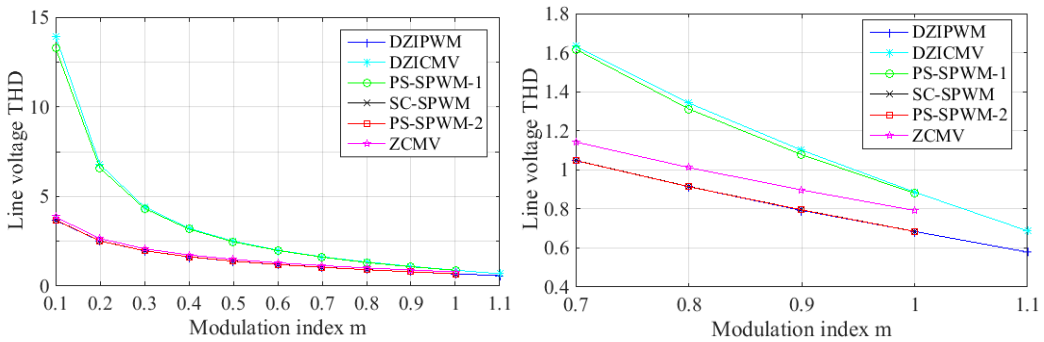

Figure 17. The THD values of line voltage u_{ab} for relative strategies: (**left**) with $0.1 < m < 1.1$ (**right**) with $0.7 < m < 1.1$.

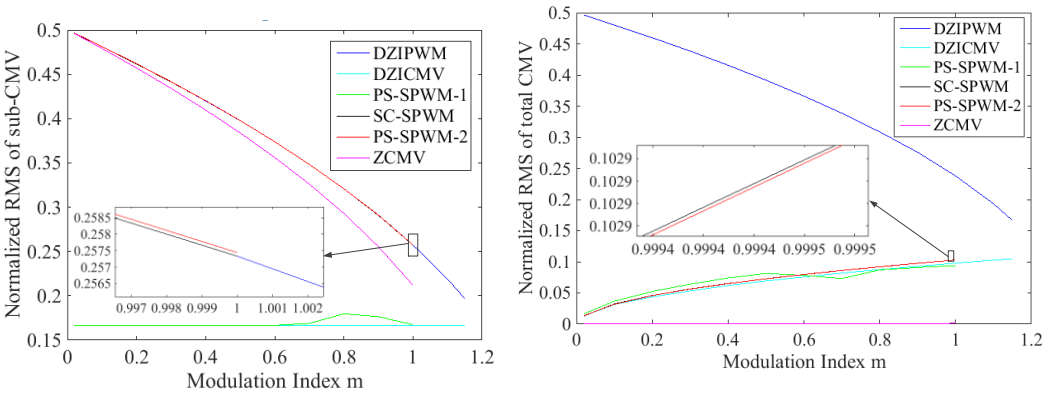

Figure 18. Normalized RMS value of CMV in simulation (**left**) sub-CMV (**right**) total CMV.

As shown in Figure 17, with the increase of m, the line voltage THD values of all these strategies are decreased. This is because the fundamental voltage rises as m increases. It should be noted that the THD value difference between DZICMV and DZIPWM is decreased when m increases. The reason is that the zero vectors (000) and (111) in each three-phase windings are eliminated by DZICMV, and thus, the harmonic distortion is decreased in the high linear modulation region. The THD values of DZICMV are very close to that of PS-SPWM-1. However, in the high linear modulation region, the CMV suppression effect of DZICMV is much better than that of PS-SPWM-1. As can be seen from Table 5, compared with PS-SPWM-1 in $0.76 < m < 1$, the peak values of sub-CMV in DZICMV can be reduced by 66.67%, and the peak values of total-CMV can be reduced by 50%. Although the line voltage THD values of other four strategies are lower than DZICMV, their sub-CMV peak values are $\pm U_{dc}/2$, which is 66.67% higher than that of DZICMV.

It can be seen from Figure 18 that the sub-CMV RMS values of the proposed DZICMV are the lowest among these strategies. The reason is that the sub-CMV values of DZICMV are $\pm U_{dc}/6$, while that of other strategies are $\pm U_{dc}/6$ and $\pm U_{dc}/2$. Therefore, their sub-CMV RMS values are larger than that of DZICMV. For $0 < m < 0.67$, the sub-CMV peak values of PS-SPWM-1 are identical to DZICMV, and thus, their sub-CMV RMS values are nearly the same. The sub-CMV RMS values of DZIPWM, PS-SPWM-2, and SC-PWM are close to each other, especially for the DZIPWM and SC-PWM. However, the total CMV RMS values of SC-PWM are significantly lower than that of DZIPWM, and they are close to PS-SPWM-2. The sub-CMV RMS values of ZCMV are medium among these strategies, while its total CMV RMS value is 0, which is the lowest. This is because the peak value of total CMV in ZCMV is 0 in theory. For the proposed DZICMV, the total CMV RMS values also perform well, which are close to PS-SPWM-2 and SC-PWM.

5. Experiment

To further validate the performance of the proposed DZICMV and other strategies, an experiment platform was built, as shown in Figure 19. This platform mainly consists of a six-phase induction motor, a load motor, a load motor driver, a power board, a control board, and a DC source. The control board is based on the Microzed evaluation board, equipped with the Xilinx Zynq System-on-Chip. It is composed of a floating-point digital signal processor (DSP) and a field programmable gate array (FPGA). The DSP is used for calculation, and the FPGA is responsible for the generation of PWM signals. The power board is implemented by the insulated gate bipolar transistor IHW30N120R2 (1200 V, 30 A, Infineon). A Switching Power Supply Weir 413D (7.5 V, 4 A) provides 5 V DC voltage for sensors. The value of DC source voltage (POWER SUPPLY EA-PS 8360-15T) was set to 360 V and the dead time was set to 2 us. Consistent with the simulation, the carrier frequency f_c was set to 5 kHz, and the control method was FOC. The motor started without any load, and a load torque of 15 N·m was assigned after the motor operates stably. This

experiment corresponds to Condition 2 of the simulation. The parameters of the motor are identical to the simulation and are listed in Table 6.

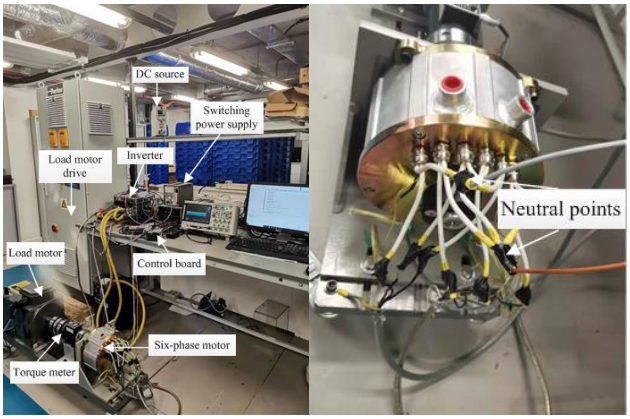

Figure 19. The experiment platform.

As shown in Figure 19, the two endpoints of every phase winding in the motor were led out, and thus, there are 12 endpoints in total for the experimental six-phase motor. Then, three endpoints were connected for each set of three-phase windings, and two neutral points were, thus, generated. Since the two neutral points are isolated from each other, it is convenient to measure the two sub-CMVs. As the total CMV cannot be measured directly, the common-mode leakage current was measured to reflect the total CMV suppression effect. The experimental sub-CMV results of DZIPWM and DZICMV are shown in Figures 20 and 21, respectively.

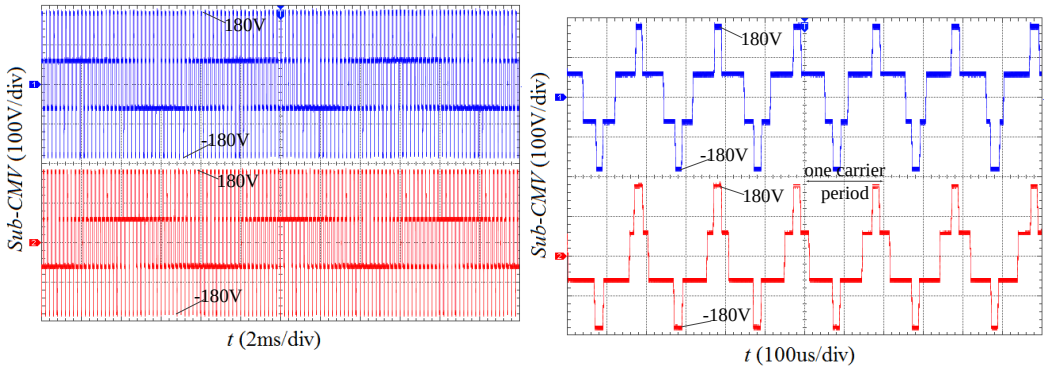

Figure 20. Experimental results of sub-CMVs for DZIPWM. (Blue line denotes the V_{cm1} and red line denotes V_{cm2}).

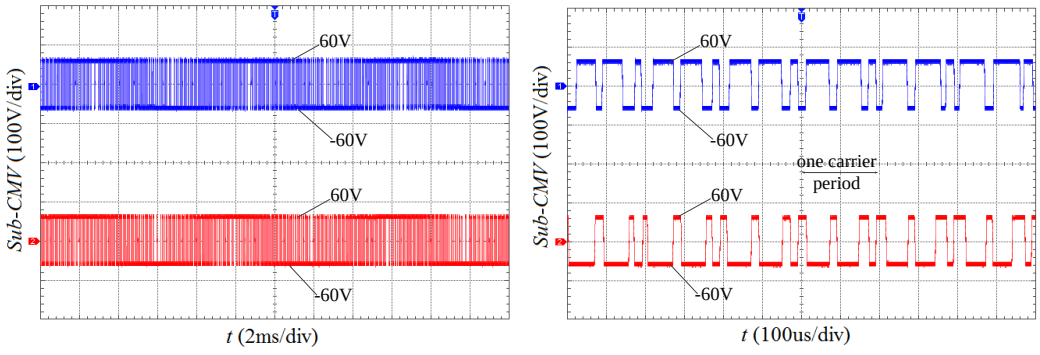

Figure 21. Experimental results of sub-CMVs for DZICMV. (Blue line denotes the V_{cm1} and red line denotes V_{cm2}).

As shown in Figures 20 and 21, the peak values of sub-CMV in DZIPWM are ±180 V, while they are only ±60 V in DZICMV. These results have verified the simulation results shown in Figures 7 and 8.

The spectral analysis of the experimental sub-CMV results for both strategies is shown in Figure 22. At the first carrier frequency sideband (5 kHz), the maximum harmonic amplitude of the DZICMV is obviously lower than that of DZIPWM, which is consistent with the simulation results.

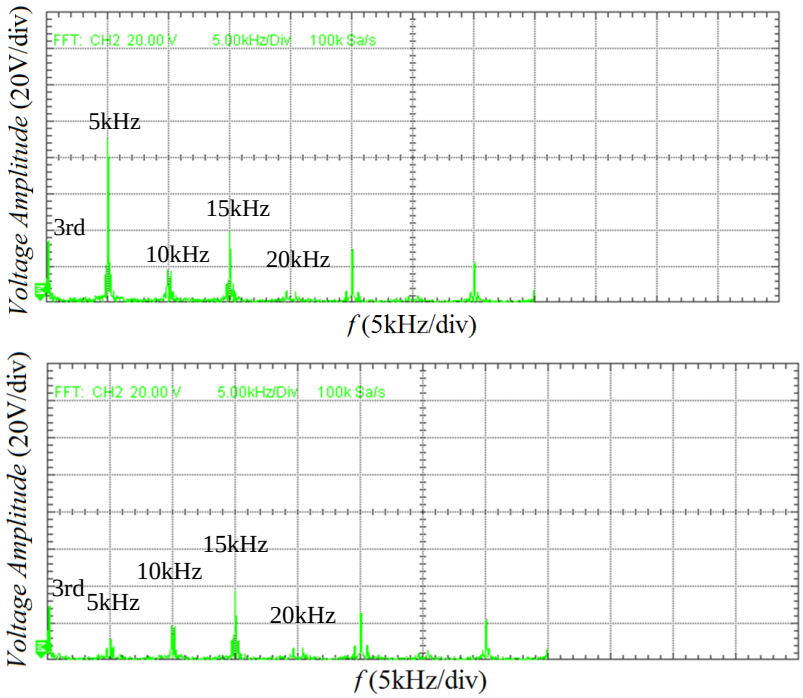

Figure 22. The spectral analysis of experimental sub-CMV results (**top**) DZIPWM; (**bottom**) DZICMV.

To further study the CMV suppression effect of the proposed DZICMV, the motor frame was connected with a copper sheet, which provided the electrical grounding to measure the common-mode leakage current. The common-mode leakage current is determined by the total CMV and the motor structural parameters. As shown in Figure 23, the leakage current peak value of DZICMV is approximately 0.1 A. The majority of peak values of DZIPWM are about 0.17 A, while a few peak values can reach 0.31 A. These high peak values in the DZIPWM are caused by transient high dv/dt of total CMV, as shown in the enlarged view of Figure 7. The leakage current RMS value of DZICMV is 0.0079 A, while that of DZIPWM is 0.0164 A. It is reduced by 51.83% in the DZICMV. Therefore, compared with the conventional DZIPWM, the proposed DZICMV can reduce the magnitude and RMS value of common-mode leakage current.

Corresponding to the simulation, the line voltage, phase current, electromagnetic torque T_e, and rotor speed n were also measured in the experiments, as shown in Figures 24–28.

In the experiment, apart from DZIPWM and DZICMV, the line voltage THD and the RMS values of sub-CMV for the four other strategies listed in Table 5 were also measured at different modulation indexes, as plotted in Figures 29 and 30. Consistent with the simulation, this experiment was applied in open-loop control, and the fundamental frequency and carrier frequency were set to 40 and 5 kHz, respectively. These measurement results of the sub-CMV RMS values were also normalized by U_{dc} = 360 V.

Overall, the experimental results are close to their simulated counterparts. The current waveforms shown in Figures 26 and 27 were measured at the motor operating in a steady state under Condition 2, and there are no significant differences between these two figures. Figure 28 shows the change of T_e and n after loading for the DZIPWM and DZICMV. Compared with the DZIPWM, the torque ripple of DZICMV is slightly larger. In addition,

due to the limitation of the large vertical axis unit (200 r·min^{-1}/div), the speed change cannot be accurately reflected, and thus, the adjustment time of speed looks to be shorter than that of torque.

As shown in Figures 29 and 30, the experimental results of the line voltage THD and sub-CMV RMS of relative strategies are close to their simulation counterparts shown in Figures 17 and 18. The sub-CMV RMS values of DZICMV are still the lowest.

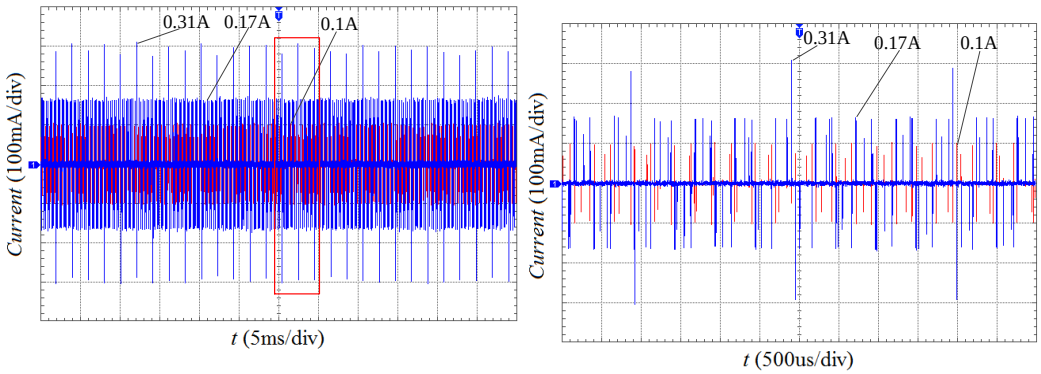

Figure 23. Experimental common-mode leakage current for DZIPWM (blue line) and DZICMV (red line). (The enlarged view of the red box in the left figure is shown in the right figure.)

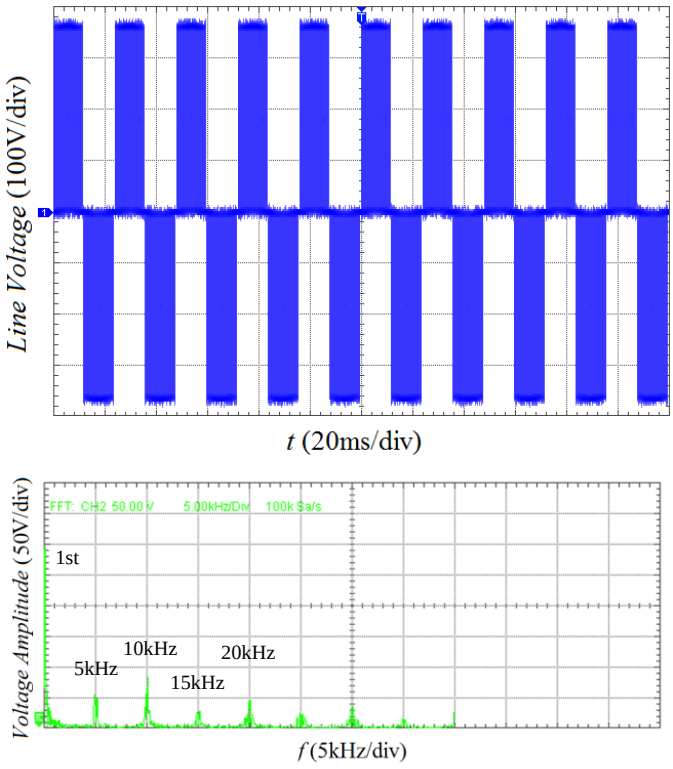

Figure 24. Experimental result of DZIPWM at m = 0.9703: (**top**) line voltage u_{ab}; (**bottom**) the FFT analysis of u_{ab}.

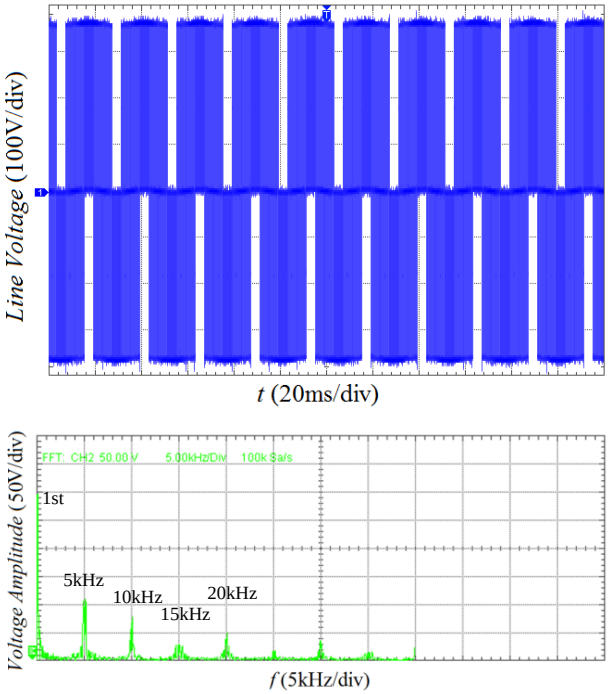

Figure 25. Experimental result of DZICMV at m = 0.9703: (**top**) line voltage u_{ab} (**bottom**) the FFT analysis of u_{ab}.

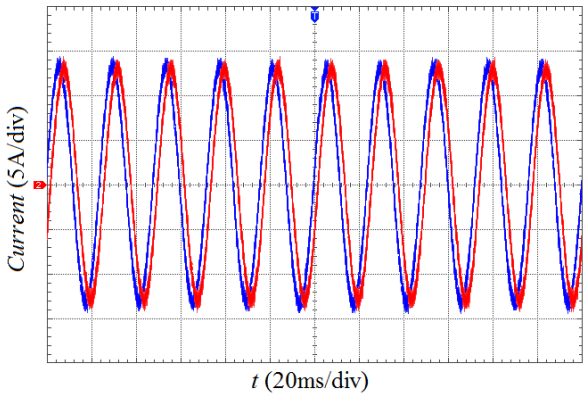

Figure 26. Experimental current waveforms of DZIPWM at m = 0.9703; current i_a (blue line) and i_u (red line).

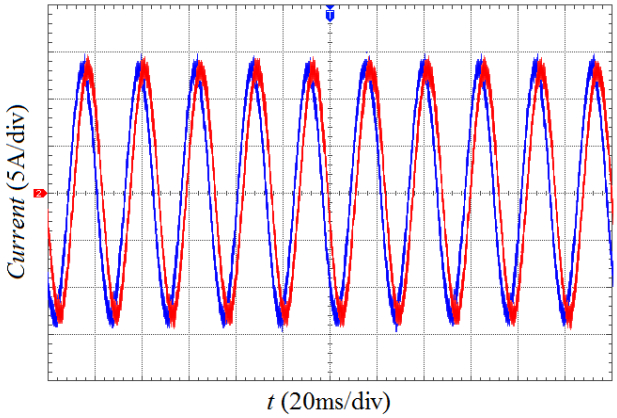

Figure 27. Experimental current waveforms of DZICMV at m = 0.9703; current i_a (blue line) and i_u (red line).

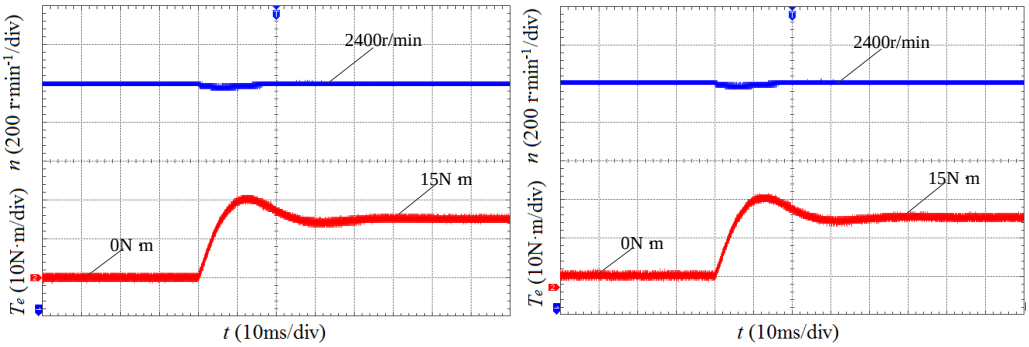

Figure 28. Experimental electromagnetic torque T_e and rotor speed n (**left**) DZIPWM; (**right**) DZICMV.

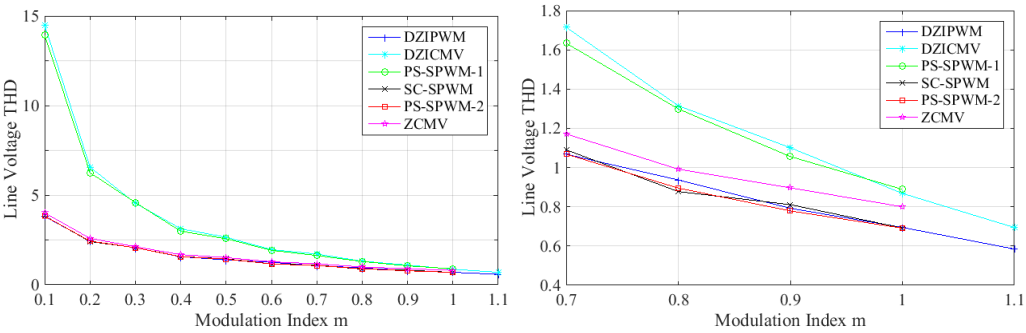

Figure 29. The experimental THD values of line voltage u_{ab} for relative strategies: (**left**) with $0.1 < m < 1.1$ (**right**) with $0.7 < m < 1.1$.

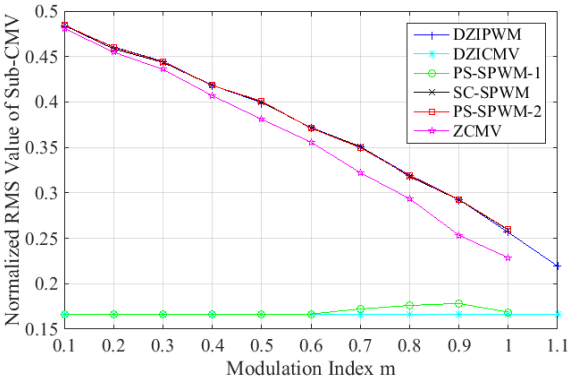

Figure 30. Normalized RMS value of sub-CMV in the experiment.

6. Conclusions

In the traditional DZIPWM, since the zero vectors for six-phase windings, namely (000000) and (111111), existed, the peak values of both sub-CMV and total CMV are $\pm U_{dc}/2$. For the two-level six-phase VSI, the possible values of sub-CMV are $\pm U_{dc}/2$ and $\pm U_{dc}/6$, and that of total CMV are $\pm U_{dc}/2$, $\pm U_{dc}/3$, $\pm U_{dc}/6$, and 0. Therefore, compared with DZIPWM, the peak values of sub-CMV can be reduced by 66.67% at most, while that of total CMV can be reduced by 33.33, 66.67 and 100%, respectively.

In this paper, a CMV suppression strategy, namely DZICMV, is proposed for two-level six-phase VSI. For the DZICMV, by eliminating zero vectors, namely (000) and (111), in each set of three-phase windings, the peak values of sub-CMV can be reduced from $\pm U_{dc}/2$ to $\pm U_{dc}/6$. Furthermore, the values of these two sub-CMVs are not always opposite, which leads to the values of total CMV being $\pm U_{dc}/6$ and 0. The combinations of sub-CMV and total CMV in DZICMV correspond to Groups 4, 5, and 6 in Table 3. Therefore, the peak values of both sub-CMV and total CMV in DZICMV are $\pm U_{dc}/6$, which is 66.67% lower than that of DZIPWM. The RMS value of the common mode leakage current was

reduced by 51.83% in the experiment. In addition, the torque and speed characteristics of these two strategies are close to each other. With the CMV decreasing, the reliability of the drive system is improved. Therefore, the DZICMV is suitable for the occasion where high reliability is required, e.g., the warships driven by a six-phase motor. The disadvantage of the proposed DZICMV is that it increases the harmonic distortion of the output voltage and current. However, this problem can be mitigated with a suitable motor design and control scheme.

Author Contributions: Formal analysis, L.Z. and Y.G.; Investigation, L.Z.; Methodology, L.Z.; Project administration, S.H.; Resources, S.H.; Supervision, S.H.; Validation, L.Z.; Visualization, and J.Z.; Writing—original draft, L.Z.; Writing—review and editing, Y.G. All authors have read and agreed to the published version of the manuscript.

Funding: This research was funded by the National Natural Science Foundation of China under grant No.51737004, the National Key Research and Development Programs under grant No. 2016YFF0203400, the National Natural Science Foundation of China under grant No. 51777064, and the Hunan Education Department Science Research Project (21C0446).

Institutional Review Board Statement: Not applicable.

Informed Consent Statement: Not applicable.

Conflicts of Interest: The authors declare no conflict of interest.

References

1. Li, S.; Zhang, S.; Habetler, T.G.; Harley, R.G. Modeling, design optimization, and applications of switched reluctance machines—A review. *IEEE Trans. Ind. Appl.* **2019**, *55*, 2660–2681. [CrossRef]
2. Matallana, A.; Ibarra, E.; Lopez, I.; Andreu, J.; Garate, J.I.; Jorda, X. Power module electronics in HEV/EV applications: New trends in wide-bandgap semiconductor technologies and design aspects. *Renew. Sustain. Energy Rev.* **2019**, *113*, 109264. [CrossRef]
3. López, I.; Ibarra, E.; Matallana, A.; Andreu, J.; Kortabarria, I. Next generation electric drives for HEV/EV propulsion systems: Technology, trends and challenges. *Renew. Sustain. Energy Rev.* **2019**, *114*, 109336. [CrossRef]
4. Electric Vehicle Outlook—Bloomberg's Forecast for Annual Electric Vehicle Sales. Available online: https://about.bnef.com/electric-vehicle-outlook/ (accessed on 16 September 2020).
5. Fernandez, M.; Sierra-Gonzalez, A.; Robles, E.; Kortabarria, I.; Ibarra, E.; Martin, J. New modulation technique to mitigate common mode voltage effects in star-connected five-phase AC drives. *Energies* **2020**, *13*, 607. [CrossRef]
6. Asefi, M.; Nazarzadeh, J. Survey on high-frequency models of PWM electric drives for shaft voltage and bearing current analysis. *IET Electr. Syst. Transp.* **2017**, *7*, 179–189. [CrossRef]
7. Plazenet, T.; Boileau, T.; Caironi, C.; Nahid-Mobarakeh, B. A comprehensive study on shaft voltages and bearing currents in rotating machines. *IEEE Trans. Ind. Appl.* **2018**, *54*, 3749–3759. [CrossRef]
8. Tufan, K. Robust stability analysis of PD type single input interval type-2 fuzzy control systems. In Proceedings of the IEEE International Conference on Fuzzy Systems (FUZZ-IEEE), Beijing, China, 6–11 July 2014; pp. 634–639.
9. Sakalli, A.; Kumbasar, T.; Jerry, M.M. Towards Systematic Design of General Type-2 Fuzzy Logic Controllers: Analysis, Interpretation, and Tuning. *IEEE Trans. Fuzzy Syst.* **2021**, *29*, 226–239. [CrossRef]
10. Tufan, K.; Hani, H. A Self-Tuning zSlices-Based General Type-2 Fuzzy PI Controller. *IEEE Trans. Fuzzy Syst.* **2015**, *23*, 991–1013.
11. Cho, S.; Jung, K.; Choi, J. Design optimization of interior permanent magnet synchronous motor for electric compressors of air-conditioning systems mounted on EVs and HEVs. *IEEE Trans. Magn.* **2018**, *54*, 1–5. [CrossRef]
12. Lei, G.; Zhu, J.; Guo, Y.; Shao, K.; Xu, W. Multiobjective Sequential Design Optimization of PM-SMC Motors for Six Sigma Quality Manufacturing. *IEEE Trans. Magn.* **2014**, *50*, 717–720. [CrossRef]
13. Huang, C.; Lee, F.; Liu, C.; Chen, J.; Lin, Y.; Yang, S. Torque Ripple Reduction for BLDC Permanent Magnet Motor Drive using DC-link Voltage and Current Modulation. *IEEE Access.* **2022**, *10*, 51272–51284. [CrossRef]
14. Akagi, H.; Doumoto, T. A Passive EMI Filter for Preventing High-Frequency Leakage Current From Flowing Through the Grounded Inverter Heat Sink of an Adjustable-Speed Motor Drive System. *IEEE Trans. Ind. Appl.* **2005**, *41*, 1215–1223. [CrossRef]
15. Son, Y.; Sul, S. A new active common-mode EMI filter for PWM inverter. *IEEE Trans. Power Electron.* **2003**, *18*, 1309–1314. [CrossRef]
16. Morris, C.T.; Han, D.; Sarlioglu, B. Reduction of common mode voltage and conducted EMI through three phase inverter topology. *IEEE Trans. Power Electron.* **2017**, *32*, 1720–1724. [CrossRef]
17. Tan, C.; Xiao, D.; Fletcher, J.E.; Rahman, M.F. Analytical and experimental comparison of carrier-based PWM methods for the five-phase coupled-inductor inverter. *IEEE Trans. Ind. Electron.* **2016**, *63*, 7328–7338. [CrossRef]

18. Hassan, M.S.; Diab, A.A.Z. Interleaved PWM Strategy for Common-Mode Leakage Current and EMI Noise Reduction of Paralleled Single-Stage DC-AC Converters. In Proceedings of the IEEE Applied Power Electronics Conference and Exposition (APEC), New Orleans, LA, USA, 15–19 March 2020; pp. 768–774.
19. Oh, H.W.; Willwerth, A.H. New motor design with conductive micro fiber shaft grounding ring prevents bearing failure in PWM inverter driven motors. In Proceedings of the Electrical Insulation Conf. and Electrical Manufacturing Expo, Nashville, TN, USA, 22–24 October 2007; pp. 199–212.
20. Adam, W.; Matthew, R. Electrical Bearing Damage—A Lurking Problem In Inverter-Driven Traction Motors. In Proceedings of the 2013 IEEE Transportation Electrification Conference and Expo (ITEC), Detroit, MI, USA, 16–19 June 2013; pp. 1–4.
21. Hoseini, S.K.; Adabi, J.; Sheikholeslami, A. Predictive modulation schemes to reduce common-mode voltage in three-phase inverters-fed AC drive systems. *IET Power Electron.* **2014**, *7*, 840–849. [CrossRef]
22. Kwak, S.; Mun, S.K. Model predictive control method to reduce common-mode voltage for three-phase voltage source inverters. *IEEE Trans. Power Electron.* **2015**, *30*, 5019–5035. [CrossRef]
23. Wu, X.; Tan, G.; Ye, Z.; Liu, Y.; Xu, S. Optimized Common-Mode Voltage Reduction PWM for Three-Phase Voltage-Source Inverters. *IEEE Trans. Power Electron.* **2016**, *31*, 2959–2969. [CrossRef]
24. Jin, H.; Shi, H.X. Suppressing low-frequency components of common-mode voltage through reverse injection in three-phase inverter. *IET Power Electron.* **2014**, *7*, 1644–1653.
25. Yang, H.; Lu, H.; Li, Y.; Chai, J. Analysis and Suppression of Common Mode Voltage for SiC Inverters in Electric Vehicle Applications. *IEEE Trans. Power Electron.* **2019**, *34*, 6276–6285.
26. Guo, F.; Yang, T.; Bozhko, S.; Wheeler, P. A Novel Virtual Space Vector Modulation Scheme for Three-Level NPC Power Converter with Neutral-Point Voltage Balancing and Common-Mode Voltage Reduction for Electric Starter/Generator System in More-Electric-Aircraft. In Proceedings of the 2019 IEEE Energy Conversion Congress and Exposition (ECCE), Baltimore, MD, USA, 29 September 2019; pp. 1852–1858.
27. Duran, M.J.; Prieto, J.; Barrero, F.; Riveros, J.A.; Guzman, H. Space-Vector PWM With Reduced Common-Mode Voltage for Five-Phase Induction Motor Drives. *IEEE Trans. Ind. Electron.* **2013**, *60*, 4030–4040. [CrossRef]
28. Muduli, U.R.; Chikondra, B.; Behera, R.K. Space Vector PWM Based DTC Scheme With Reduced Common Mode Voltage for Five-Phase Induction Motor Drive. *IEEE Trans. Power Electron.* **2022**, *37*, 114–124. [CrossRef]
29. Yu, B.; Song, W.; Guo, Y.; Li, J.; Saeed, M.S.R. Virtual Voltage Vector-Based Model Predictive Current Control for Five-Phase VSIs With Common-Mode Voltage Reduction. *IEEE Trans. Transp. Electrif.* **2021**, *7*, 706–717. [CrossRef]
30. Bhowate, A.; Aware, M.V.; Sharma, S. Predictive Torque Control of Five-Phase Induction Motor Drive Using Successive Cost Functions for CMV Elimination. *IEEE Trans. Power Electron.* **2021**, *36*, 14133–14141. [CrossRef]
31. Wang, F.; Wallace, A.; Dai, S.; Von Jouanne, A.; Zhang, H. Multilevel Inverter Modulation Schemes to Eliminate Common-Mode Voltages. *IEEE Trans. Ind. Appl.* **2000**, *36*, 1645–1653. [CrossRef]
32. Nguyen, N.-V.; Nguyen, T.-K.T.; Lee, H.-H. A Reduced Switching Loss PWM Strategy to Eliminate Common-Mode Voltage in Multilevel Inverters. *IEEE Trans. Power Electron.* **2015**, *30*, 5425–5438. [CrossRef]
33. Acosta-Cambranis, F.; Zaragoza, J.; Berbel, N.; Capella, G.; Martinez, J.L.R. Constant Common-Mode Voltage Strategies Using Sigma-Delta Modulators in Five-Phase VSI. *IEEE Trans. Ind. Electron.* **2022**. [CrossRef]
34. Acosta-Cambranis, F.; Zaragoza, J.; Berbel, N.; Capella, G.J.; Martinez, L.R. Common-Mode Voltage Mitigation Strategies Using Sigma-Delta Modulation in Five-Phase VSIs. *IEEE Trans. Power Electron.* **2022**, *37*, 11662–11672. [CrossRef]
35. Robles, E.; Fernandez, M.; Andreu, J.; Ibarra, E.; Zaragoza, J.; Ugalde, U. Common-mode voltage mitigation in multiphase electric motor drive systems. *Renew. Sustain. Energy Rev.* **2022**, *157*, 111971. [CrossRef]
36. Liu, Z.; Zheng, Z.; Scott, D.S.; Gu, C.; Li, Y. Reduction of Common-Mode Voltage in Multiphase Two-Level Inverters Using SPWM With Phase-Shifted Carriers. *IEEE Trans. Power Electron.* **2016**, *31*, 6631–6645. [CrossRef]
37. Liu, Z.; Zheng, Z.; Peng, Z.; Li, Y.; Hao, L. A Sawtooth Carrier-Based PWM for Asymmetrical Six-Phase Inverters With Improved Common-Mode Voltage Performance. *IEEE Trans. Power Electron.* **2018**, *33*, 9444–9458. [CrossRef]
38. Shen, Z.; Jiang, D.; Liu, Z.; Ye, D.; Li, J. Common-Mode Voltage Elimination for Dual Two-Level Inverter-Fed Asymmetrical Six-Phase PMSM. *IEEE Trans. Power Electron.* **2020**, *35*, 3828–3840. [CrossRef]
39. Zhou, C.; Yang, G.; Su, J. PWM Strategy With Minimum Harmonic Distortion for Dual Three-Phase Permanent-Magnet Synchronous Motor Drives Operating in the Overmodulation Region. *IEEE Trans. Power Electron.* **2016**, *31*, 1367–1380. [CrossRef]
40. Zhao, Y.; Lipo, T.A. Space vector PWM control of dual three-phase induction machine using vector space decomposition. *IEEE Trans. Ind. Appl.* **1995**, *31*, 1100–1109. [CrossRef]
41. Marouani, K.; Baghli, L.; Hadiouche, D.; Kheloui, A.; Rezzoug, A. A New PWM Strategy Based on a 24-Sector Vector Space Decomposition for a Six-Phase VSI-Fed Dual Stator Induction Motor. *IEEE Trans. Ind. Electron.* **2008**, *55*, 1910–1920. [CrossRef]
42. Hava, A.M.; Kerkman, R.; Lipo, T.A. Simple analytical and graphical methods for carrier-based PWM-VSI drives. *IEEE Trans. Power Electron.* **1999**, *14*, 49–61. [CrossRef]